UNIVERSITY OF CRETE

SCHOOL OF SCIENCES AND ENGINEERING

DEPARTMENT OF MATERIALS SCIENCE AND TECHNOLOGY

Master Thesis

MESOPOROUS NETWORKS OF MoS_2 AND CdS NANOPARTICLES AS PHOTOCATALYSTS FOR WATER SPLITTING AND HYDROGEN PRODUCTION

Patriarchea Chrysanthi

Supervisor: Prof. Gerasimos S. Armatas

HERAKLION 2021

ΠΑΝΕΠΙΣΤΗΜΙΟ ΚΡΗΤΗΣ
ΣΧΟΛΗ ΘΕΤΙΚΩΝ ΚΑΙ ΤΕΧΝΟΛΟΓΙΚΩΝ ΕΠΙΣΤΗΜΩΝ
ΤΜΗΜΑ ΕΠΙΣΤΗΜΗΣ ΚΑΙ ΤΕΧΝΟΛΟΓΙΑΣ ΥΛΙΚΩΝ

Μεταπτυχιακή Διατριβή

ΜΕΣΟΠΟΡΩΔΗ ΔΙΚΤΥΑ ΝΑΝΟΣΩΜΑΤΙΔΙΩΝ MoS_2 ΚΑΙ CdS ΩΣ ΦΩΤΟΚΑΤΑΛΥΤΕΣ ΓΙΑ ΤΗ ΔΙΑΣΠΑΣΗ ΤΟΥ ΝΕΡΟΥ ΠΡΟΣ ΠΑΡΑΓΩΓΗ ΥΔΡΟΓΟΝΟΥ

Πατριαρχέα Χρυσάνθη

Υπεύθυνος Καθηγητής: Αρματάς Σ. Γεράσιμος

ΗΡΑΚΛΕΙΟ 2021

Master's Examining Committee

Armatas Gerasimos

Associate Professor, Department of Materials Science and Technology,

University of Crete

Remediakis Ioannis

Associate Professor, Department of Materials Science and Technology,

University of Crete

Stoumpos Constantinos

Associate Professor, Department of Materials Science and Technology,

University of Crete

Acknowledgements

"*I am among those who think that science has great beauty. A scientist in his laboratory is not only a technician: he is also a child placed before natural phenomena which impress him like a fairy tale.*"
-Marie Curie

This research was carried out in the Laboratory of Advanced Materials Chemistry at the University of Crete's Department of Materials Science and Technology for the fulfillment of the requirements for the Master of Science degree. First and foremost, I would like to convey my sincere gratitude and appreciation to Professor Gerasimos Armatas. From the beginning, he provided me with all the means to conduct top-notch research in his highly equipped laboratory, and I am deeply grateful for his continued guidance and encouragement. Without his inspirational ideas and insightful discussions, this research could not have been completed. Moreover, I wish to express my warm thanks to all my collaborators and colleagues, especially to Dr. Eirini Koutsouroumpi, Dr. Ioannis Vamvasakis and Mr. Evangellos Andreou, whom I have the privilege to call my friends. Their expertise, knowledge and experience with various laboratory techniques made a significant contribution to my research. Last, but by no means least, I wish also to deeply thank Prof. George Kiriakidis, Prof. Nikolaos Pelekanos, Prof. Ioannis Remediakis and Prof. Constantinos Stoumpos for their insightful evaluation and unwavering support. I feel blessed that I have met and worked with all these one-of-a-kind people, and I would like to thank everyone who gave me this opportunity, especially my family.

Funding

The present research work was financially supported from the Hellenic Foundation for Research and Innovation (H.F.R.I.) under the “1st Call for H.F.R.I. Research Projects to support Faculty Members & Researchers and the Procurement of High-cost research equipment grant” (project number: 400).

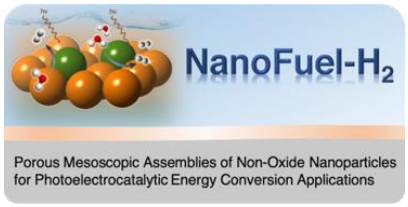

Table of Contents

Abstract

Hydrogen production by water-splitting photocatalysis has attracted significant interest in recent years as a low-cost and environmentally friendly process. Generally, a tremendous number of semiconductors have been developed that fulfil the criteria of effective photocatalysts such as appropriate band gap (1.23–3.26 eV) and suitable reduction and oxidation band position. However, due to the fast recombination process of the photoinduced carriers and low efficiency of the photon to hydrogen conversion, it is essential to construct new heterostructures with intimate contact between the components and pronounced visible-light absorption for achieving high photocatalytic performance. This thesis focuses on synthesis and characterization of new mesoporous heterojunction networks consisted of ultrasmall MoS_2 nanolayers (ca. 10–15 nm in lateral size) and sub 5 nm sized CdS nanocrystals. The application of these nanostructures as photocatalysts for H_2 generation from water splitting is also studied. To prepare these nanocomposite materials we used a polymer-templated oxidative aggregating method for CdS nanocrystal assemblies followed by a wet-chemical deposition of exfoliated MoS_2 nanosheets on CdS surface. The chemical composition and the morphological and structural properties of the catalysts were investigated with electron microprobe analysis (EDS), X-ray diffraction (XRD), X-ray photoelectron spectroscopy (XPS), electron microscopy (TEM) and N_2 physisorption. The results indicated that the MoS_2-modified CdS nanocatalysts consist of a porous network of connected cubic CdS nanocrystals and 2H-phase MoS_2 nanosheets and exhibit large internal BET surface area (ca. 159–225 $m^2 g^{-1}$) and uniform pores (ca. 6–9 nm in diameter). Photocatalytic H_2 evolution experiments coupled with UV–vis/NIR absorption, time-resolved photoluminescence (TRPL) and electrochemical impedance spectroscopy (EIS) measurements revealed that the superior photocatalytic activity in

these materials arises from the efficient dissociation and transport of photogenerated charge carriers across the nanoscale MoS_2/CdS junctions and the large number of exposed active sites due to the 3D open-pore structure. The optimized MoS_2/CdS catalyst at 20 wt.% MoS_2 content achieves a H_2 evolution rate of ~0.4 mmol h^{-1} (or ~19 mmol h^{-1} g^{-1} mass activity) under visible light irradiation, which is 6.7 times higher than that of unmodified mesoporous CdS. We also obtained an apparent quantum yield (AQY) of 51.2% for hydrogen generation reaction using monochromatic light of 420 nm. The results of this study present an understanding of the charge transfer dynamics at the MoS_2/CdS nanoscale junctions and support the potential viability of the MoS_2-modified CdS nano-heterostructures as photocatalysts for clean energy conversion.

Περίληψη

Η παραγωγή υδρογόνου με φωτοκαταλυτική διάσπαση του νερού έχει προσελκύσει σημαντικό ενδιαφέρον τα τελευταία χρόνια ως μια διαδικασία χαμηλού κόστους και φιλική προς το περιβάλλον. Γενικά, έχει αναπτυχθεί μια πληθώρα ημιαγώγιμων υλικών που πληρούν τα κριτήρια ενός αποτελεσματικού φωτοκαταλύτη, όπως το κατάλληλο ενεργειακό χάσμα (1.23–3.26 eV) και τα κατάλληλα δυναμικά οξείδωσης και αναγωγής. Ωστόσο, λόγω της γρήγορης επανασύνδεσης των φωτοδιεγερμένων φορέων και της χαμηλής απόδοσης μετατροπής φωτονίων σε υδρογόνο, είναι απαραίτητο να κατασκευαστούν νέες ετεροδομές με στενή επαφή μεταξύ των συστατικών τους και έντονη απορρόφηση στο φάσμα του ορατού ώστε να επιτευχθεί υψηλή φωτοκαταλυτική αποτελεσματικότητα. Η μεταπτυχιακή αυτή εργασία επικεντρώνεται στη σύνθεση και το χαρακτηρισμό νέων μεσοπορώδων νανο-ετεροδομών που αποτελούνται από μικρού μεγέθους νανοφύλλα MoS_2 (περίπου 10–15 nm σε διάμετρο) και νανοκρυστάλλους CdS μεγέθους κάτω από 5 nm. Μελετάται επίσης η δυνατότητα εφαρμογής αυτών των ετεροδομών ως φωτοκαταλύτες στην παραγωγή H_2 από τη φωτοχημική διάσπαση του νερού. Για την ανάπτυξη των υλικών αυτών χρησιμοποιήθηκε αρχικά ήπιος οξειδωτικός πολυμερισμός κολλοειδών νανοσωματιδίων CdS παρουσία οργανικού πολυμερούς και ακολούθησε χημική εναπόθεση αποφλοιωμένων νανοφύλλων MoS_2 στην επιφάνεια του CdS. Η χημική σύσταση και οι μορφολογικές και δομικές ιδιότητες των καταλυτών διερευνήθηκαν με στοιχειακή ανάλυση EDS, περίθλαση ακτίνων-Χ (XRD), φασματοσκοπία φωτοηλεκτρονίου από ακτίνες-Χ (XPS), ηλεκτρονική μικροσκοπία διέλευσης (TEM) και ποροσιμετρία N_2. Τα αποτελέσματα έδειξαν ότι οι νανοκαταλύτες MoS_2/CdS αποτελούνται από ένα πορώδες δίκτυο συνδεδεμένων κυβικών νανοκρυστάλλων CdS και νανοφύλλων MoS_2 με εξαγωνική κρυσταλλική δομή (2H φάση), και παρουσιάζουν

μεγάλη εσωτερική επιφάνεια BET (~159–225 m^2 g^{-1}) με ομοιόμορφους πόρους (διαμέτρου ~6–9 nm). Πειράματα φωτοκαταλυτικής εξέλιξης H_2 σε συνδυασμό με μετρήσεις φασματοσκοπίας οπτικής απορρόφησης UV-vis/NIR, χρόνο-εξαρτημένης φωτοφωταύγειας (TRPL) και ηλεκτροχημικής εμπέδησης (EIS) έδειξαν ότι η αυξημένη φωτοκαταλυτική δράση των υλικών αυτών οφείλεται στον αποτελεσματικό διαχωρισμό και τη μεταφορά των φωτοδιεγερμένων φορέων φορτίου στις νανοεπαφές MoS_2/CdS καθώς και στον μεγάλο αριθμό των εκτεθειμένων ενεργών κέντρων λόγω της τρισδιάστατης δομής ανοιχτού πόρου. Ο βέλτιστος καταλύτης MoS_2/CdS με συγκέντρωση 20 wt.% MoS_2 παρουσίασε ένα μέσο ρυθμό παραγωγής H_2 ~0.4 mmol h^{-1} (ή ~19 mmol h^{-1} g^{-1}) κάτω από ακτινοβολία ορατού φωτός, ο οποίος είναι 6.7 φορές υψηλότερος από αυτόν του μη-τροποποιημένου μεσοπορώδους CdS. Επίσης, η κβαντική απόδοση (AQY) της αντίδρασης παραγωγής υδρογόνου υπολογίστηκε ίση με 51.2% χρησιμοποιώντας μονοχρωματική ακτινοβολία μήκους κύματος λ = 420 nm. Τα αποτελέσματα αυτής της μελέτης παρουσιάζουν μια εικόνα της δυναμικής μεταφοράς φορτίου στις επαφές νανοκλίμακας μεταξύ MoS_2 και CdS και υποδεικνύουν τη βιωσιμότητα των νανο-ετεροδομών MoS_2/CdS ως φωτοκαταλύτες για τεχνολογίες μετατροπής καθαρής ενέργειας.

1. Introduction

1.1 Metal chalcogenide semiconductors

Metal chalcogenides are inorganic compounds containing in their structure at least one chalcogen anion and one cation of an electro-positive element. They are commonly known as sulfides, selenides, tellurides, when their chalcogen atom is sulfur (S), selenium (Se) or tellurium (Te), respectively. According to the different stoichiometric proportions, they can be expressed with the chemical formulas MQ, MQ_2, MQ_3 (or M_2Q_3), where M represents the metal element and Q represents the chalcogen. These materials have received widespread attention from researchers due to their higher electrical conductivity and lower cost compared to the metal oxides and pure precious metals. The unique physical and chemical properties of metal chalcogenides, such as high electron transport behavior, easily regulated band structure, visible light absorption and large-scale synthesis, are very promising for applications in fields related to semiconductor electronics, optoelectronics, energy conversion and environment remediation.[1] In general, metal chalcogenides can be classified into two main categories: layered and nonlayered structures.[2]

Layered metal chalcogenides consist of the family of transition metal dichalcogenides or TMDs, whose generalized formula is MQ_2, where M is a transition metal and Q is a chalcogen. In these layered materials, the in-plane atoms connect to each other by strong chemical bonding in each layer, while the layers stack together through weak van den Waals interactions to form bulk crystals. Each layer typically has a thickness of 6–7 Å, which consists of a hexagonally packed layer of metal atoms sandwiched between two layers of chalcogen atoms. The intralayer M-Q bonds are predominantly covalent in nature, whereas the sandwich layers are coupled by weak

van der Waals forces, thus allowing the crystal to readily cleave along the layer surface. TMDs exhibit a wide variety of polymorphs and the most common are 1T, 2H and 3R, where the letters stand for trigonal, hexagonal and rhombohedral structure, respectively, and the digit indicates the number of Q-M-Q units in the unit cell. [3]

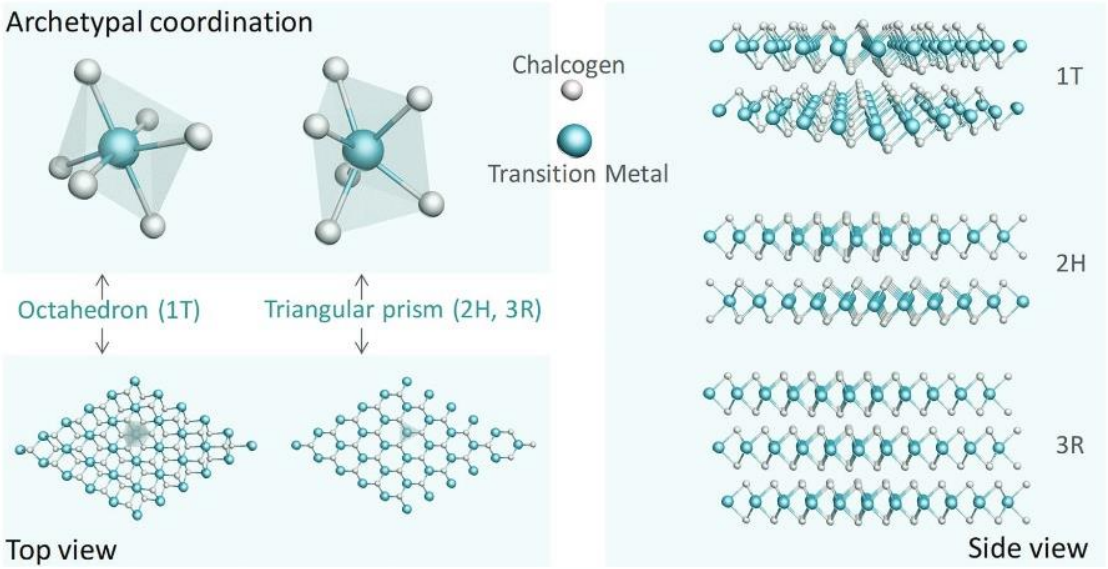

Figure 1. The typical 1T, 2H, 3R structures of TMDs.[4]

Depending on the particular combination of transition metal (group IV, V, VI, VII, IX, X) and chalcogen (S, Se, or Te) elements, the thermodynamically stable structure is either the 2H or 1T phase. For example, some of the TMDs formed by group VI transition metals (M = Mo or W; Q = S, Se or Te) are thermodynamically stable in the 2H phase and the 1T phase can be obtained as a metastable phase. In this thermodynamically stable 2H phase, these materials are semiconductors. The band structures of materials can be calculated from first principles, density functional theory (DFT), to reveal their electronic structure. In Figure **2,** it is shown the theoretical calculations for the band structure of 2H-MoS_2. It is revealed that the positions of the valence and conduction band edges changes with decreasing thickness, and the indirect bandgap semiconductor bulk material turns into a direct bandgap semiconductor

monolayer. The calculated values for the bandgap of bulk and monolayer 2H-MoS_2 are 1.2 eV and 1.9 eV, respectively.

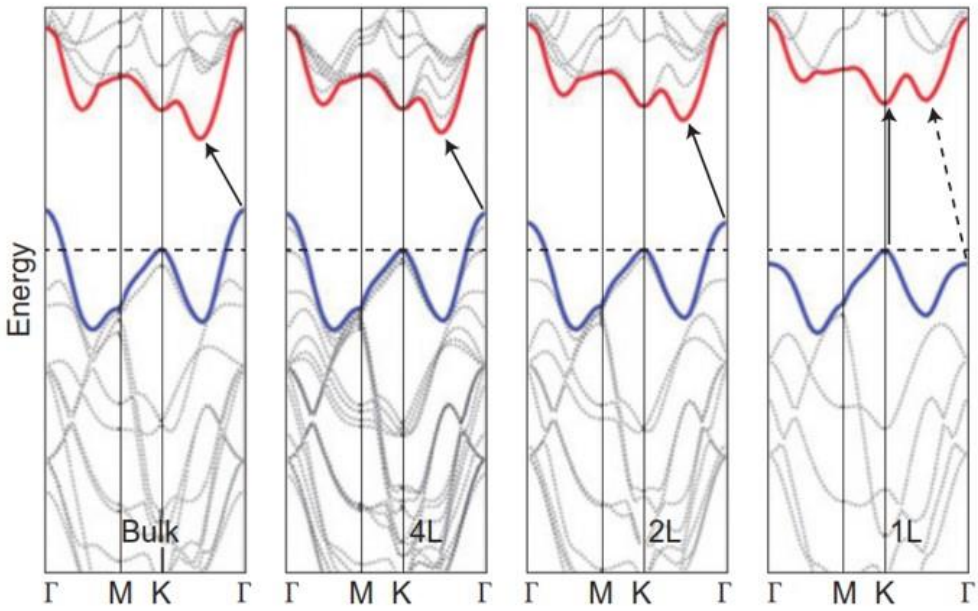

Figure 2. The evolution of the band structure of 2H-MoS_2 calculated for sample of decreasing thickness.[5]

Unlike layered metal chalcogenides, nonlayered metal chalcogenides crystallize in three dimensions (3D) via chemical bonding. They exist in a wide variety of crystal structures, depending on the coordination modes between atoms and the arrangement of atoms in the crystal lattice. Among these, the porous metal chalcogenide materials often possess interesting optoelectronic and pore surface properties as they have large internal surface area, and high ionic conductivity and framework charge density. Moreover, these materials have wide variations in their energy gaps ranging from mid-to-near infrared (PbS, PbSe and PbTe) to the visible (CdS, CdSe and CdTe) and into the ultraviolet (ZnS and ZnSe) regions. Further, this family of semiconductors possesses a reasonably high optical absorption coefficient as compared to the other class of semiconductor materials. Among all different semiconductors of nonlayered chalcogenides, cadmium sulfide (CdS) is of significant importance. In bulk form it is a

yellow-colored compound with a direct band gap of 2.4 eV and it has two distinct crystallographic structures, one hexagonal-wurtzite and another cubic-zinc blende structure.

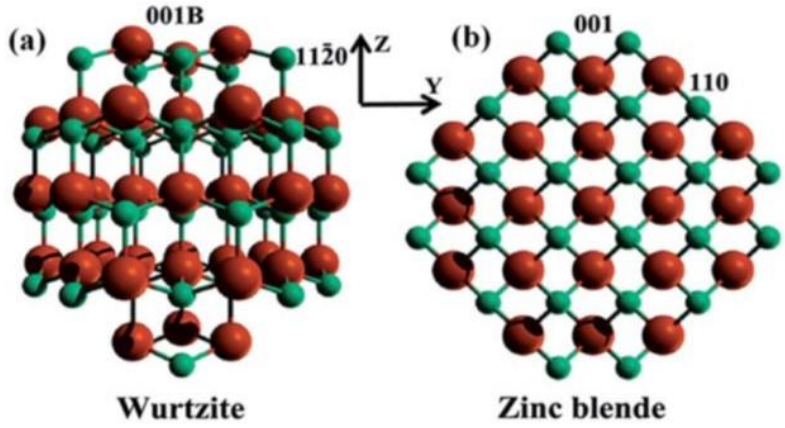

Figure 3. The crystal structures of (a) wurtzite and (b) zinc blende CdS. The red spheres represent Cd and green spheres represent S.[6]

Alongside an increasing interest in metal chalcogenides due to their intriguing and tunable properties, the range of different methods, including top-down (e.g., mechanical and chemical exfoliation) and bottom-up (e.g., chemical vapor deposition and wet-chemical synthesis) synthesis, for accessing metal chalcogenides with well-defined structures and morphologies has been growing over the years. In general, top-down synthetic processes are restricted to the design of layered metal chalcogenides that can be cleaved from their bulk crystal. On the other hand, wet-chemical syntheses (e.g., self-assembly method, hydrothermal method, ion exchange method), whose reaction parameters can be precisely tuned, have been particularly used for the preparation of nonlayered metal chalcogenides. The relatively low temperature in solution based-reaction usually leads to the formation of amorphous or low-crystalline structures, which might affect their optoelectronic and photocatalytic performance due to the presence of abundant defects. Since the band structure of layered metal

chalcogenides is dependent from their thickness, which varies with the number of layers, precise control of their electronic structure is highly possible using suitable synthesis strategies. For nonlayered structures, band structure engineering can be usually realized via doping, introduction of defects and construction of heterostructures.

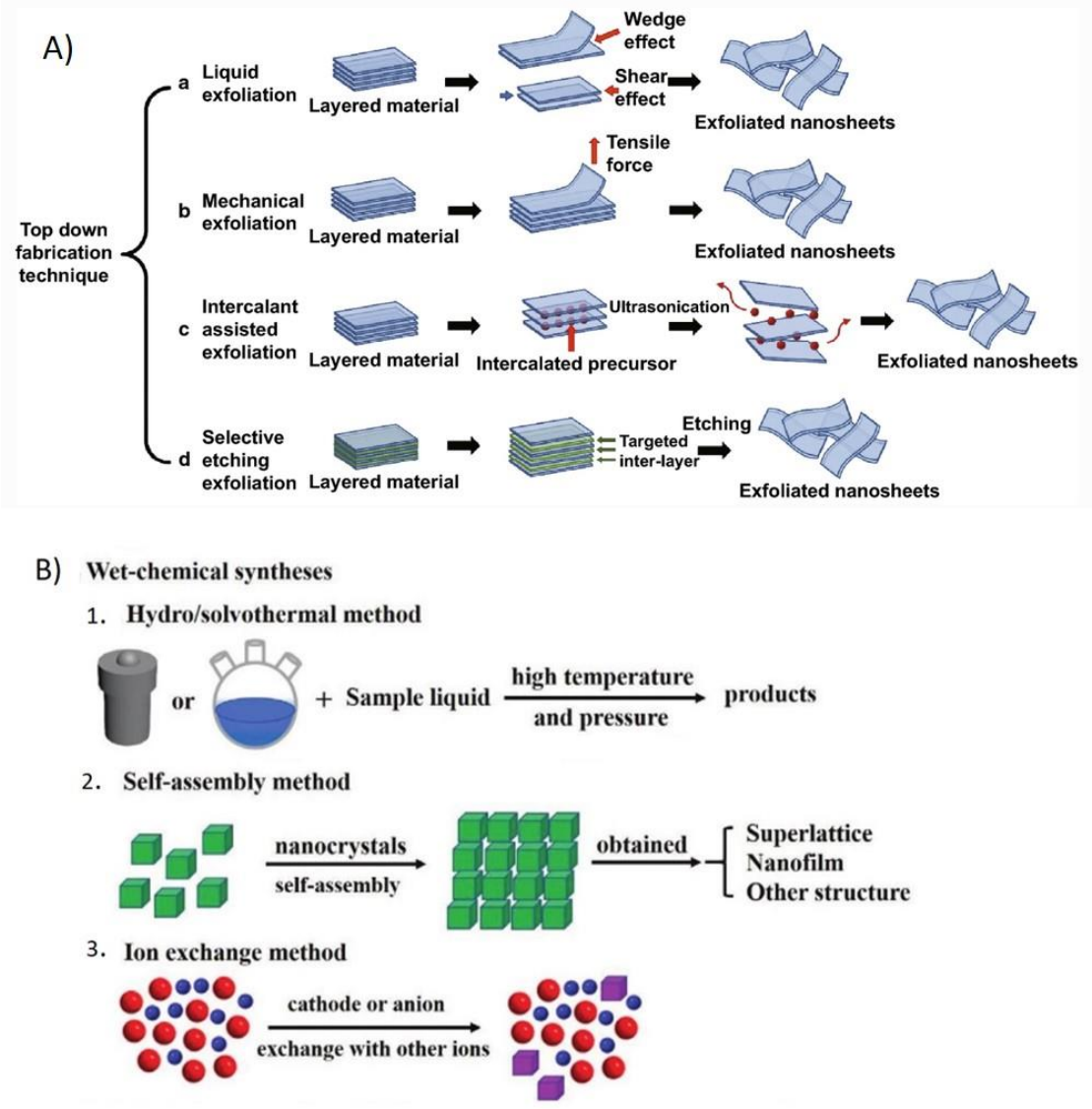

Figure 4. Schematic representation of various (A) "top-down" fabrication techniques for layered metal chalcogenides[7] and (B) wet-chemical techniques for nonlayered metal chalcogenides[8].

1.2 Photocatalytic hydrogen production

Hydrogen (H_2), which has a high energy density per unit weight (120 MJ or 33.6 kWh per Kg), is considered one of the promising energy carriers for storing solar energy in the form of chemical bond energy. Among various methods, hydrogen production by water-splitting photocatalysis is of growing interest as a low-cost and environmentally friendly process.[9] In 1972, Honda and Fujishima first demonstrated that a single-crystalline TiO_2 (rutile) achieved hydrogen production from water under ultraviolet (UV) irradiation.[10] Since then, semiconductor photocatalysis, has become a field of intense research interest and exhibits a variety of practical applications in industrial activities, such as organic pollutants mineralization, decontamination of water and wastewater effluents, production of renewable fuels (e.g., hydrogen and methane), and organic fine synthesis (e.g., hydroamination of alkynes). The overall water splitting reaction is composed of two half-reactions, the hydrogen evolution reaction (HER) and the oxygen evolution reaction (OER):

(HER) $2H^+ + 2e^- \rightarrow H_2(g)$ $\qquad E^O_{red} = 0.0\ V$

(OER) $2\ H_2O\ (l) + 4h^+ \rightarrow O_2(g) + 4H^+$ $\qquad E^O_{ox} = 1.23\ V$

(Overall water-splitting) $2\ H_2O\ (l) \xrightarrow{\text{catalyst}} H_2(g) + O_2(g)$ $\qquad \Delta E^O = 1.23\ V$

It is recognized that water splitting into H_2 and O_2 occurs on semiconductor surfaces irradiated with photons of appropriate energy. Specifically, semiconductors combine a variety of properties such as light absorption, band edge structure, charge transport and excited-state lifetimes, thus they can be leverages as photocatalysts. A semiconductor material is nonconductive in ground state because an energy gap, the bandgap (E_g), exists between the top of the filled valence band (VB) and the bottom of the vacant conduction band (CB). Consequently, electron transport between valence and

conduction band can occurs only with appropriate energy absorption. As depicted in Figure **5,** in semiconductor photocatalysis, electrons get excited from the VB to the CB when a photon with energy equal to or higher than the semiconductor bandgap is absorbed. This process creates an electronic vacancy or hole (h+) at the VB and a photogenerated electron (e^-) in the CB edge of the semiconductor. The light-induced generation of an electron-hole pair (exciton) is a required step in all semiconductor photocatalytic processes. These photogenerated species, when transferred to the solid/liquid interface, are capable of reducing and oxidizing a surface-absorbed substrate, whereas in the absence of suitable scavengers/electrolytes, electron-hole pair may undergo recombination on the surface within a few nanoseconds.

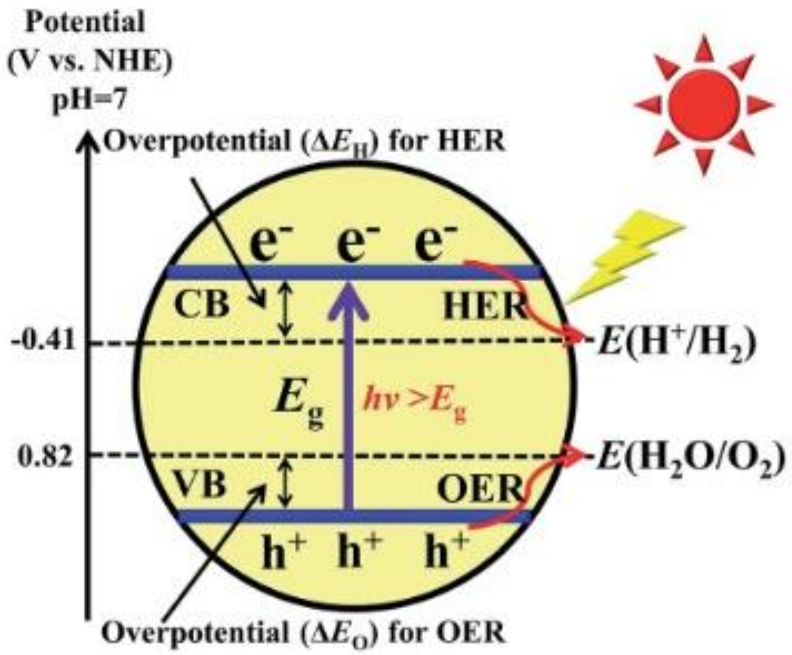

Figure 5. Photocatalytic water-splitting mechanism by a semiconductor photocatalyst.[11]

The photocatalysis is chemically productive when the electron-hole pair recombination is suppressed. CB electrons and VB holes can be separated efficiently in the presence of an intrinsic electric field, such as the one formed spontaneously in the

space-charge region at the semiconductor/liquid or semiconductor/metal (Schottky) interfaces. In this case the lifetime of photoinduced carriers increases, enhancing the possibility for electrons and holes to be involved in redox reactions on the photocatalyst surface. Interfacial electron transfer, that is transfer of an electron between the substrate and the semiconductor surface, is a crucial step towards photocatalysis. Notably, the efficiency of this step determines to a large extent the ability of the semiconductor material to serve as a catalyst for a given redox transformation.

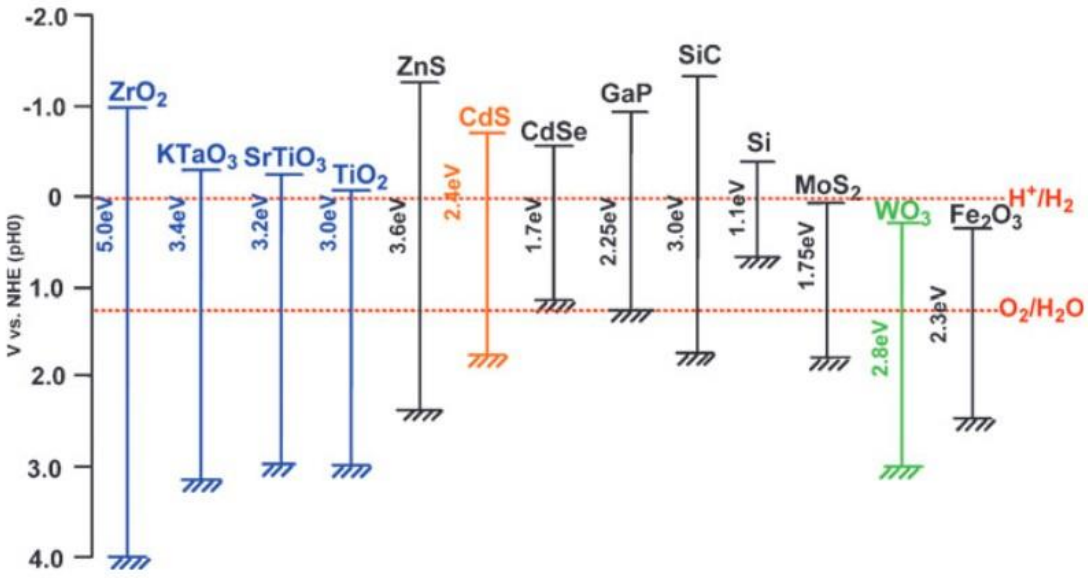

Figure 6. Band gaps and band edge positions of representative semiconductors in relation to the redox potentials for water splitting at pH=0.[12]

The position of semiconductor's conduction and valence band edges relative to the redox potentials of the adsorbed substrates (reactants) determines the efficiency of the aforementioned electron transfer reactions. As shown in Figure **6**, in order for an electron transfer reaction to occur, the potential of the electron acceptor should be located below (to a more positive direction) the CB of the semiconductor, whereas the potential of the electron donor should be located above (to a more negative direction) the VB of the semiconductor. More specifically, the photocatalyst's CB edge (or the

flat-band potential) must be located at a more negative position than the redox potential of H^+/H_2 pair (i.e., 0 V vs NHE at pH=0) for HER, while the VB edge must be more positive than the oxidation potential of H_2O to O_2 (i.e., 1.23 V vs NHE at pH=0) for OER.

2. Thesis Objective

Hydrogen production via photocatalytic water splitting using sunlight has an enormous potential to solve the worldwide energy and environmental problems. However, the efficiency of solar-water-splitting systems is still low for practical applications, which requires the construction of novel, more complicated semiconductor catalysts. In this direction, this thesis focuses on the synthesis and characterization of nanostructured MoS_2-modified mesoporous architectures of connected CdS nanocrystals as potential candidates for photocatalytic hydrogen production, providing an insightful study of the effect of MoS_2 nanosheets on the overall photocatalytic reaction.

Briefly, the specific aims of this scientific research are:

- To develop high-surface-area mesoporous CdS nanostructures and modify them with exfoliated MoS_2 nanolayers.
- To characterize the as-synthesized materials in terms of structural, morphological, optical and electrochemical properties.
- To evaluate the visible-light-driven photocatalytic activity of the newly developed MoS_2/CdS catalysts in photocatalytic production of H_2 from water splitting.
- To investigate the charge transfer dynamics and the mechanism of hydrogen evolution reaction on MoS_2/CdS heterostructures and to clarify the effect of MoS_2 nanolayers on the photocatalytic processes.

3. Experimental Section

3.1 Synthetic procedure of materials

3.1.1 Synthesis of CdS NCs

CdS nanocrystals (NCs) with 4–5 nm diameter were prepared according to a previously reported method.[13-14] In a typical procedure, 7 mmol of $CdCl_2$ and 7 mmol of $Na_2S{\cdot}9H_2O$ were dissolved separately in 50 mL and 20 mL of deionized (DI) water, respectively. After complete dissolution, 15 mmol of 3-mercaptopropionic acid (3-MPA) were slowly added into the $CdCl_2$ solution and the mixture was left under continuous stirring for 15 min at room temperature (RT). Next, ammonium hydroxide (NH_4OH) was utilized to adjust the pH at 9–10. Finally, the Na_2S solution was gradually added and the resulted yellow colloidal sol was left under continuous stirring at RT for an additional 1 h. The MPA-capped CdS NCs were isolated by precipitation with the addition of 60 mL 2-propanol, followed by centrifugation and drying at 40 ºC overnight.

3.1.2 Preparation of mesoporous CdS NCAs

The procedure for mesoporous CdS NC assemblies (NCAs) was based on our previously reported work.[15-16] Briefly, 2.0 mmol of MPA-capped CdS NCs were first dispersed in 2.5 mL DI water under stirring at RT. Then, few drops of NH_4OH were added until a clear colloid solution was observed. Next, this colloid sol was dropped into a 2.5 mL aqueous solution containing Pluronic F-127 (10% w/v) and the resulting mixture was kept under stirring for 1 h at RT. Finally, ~1 mL of a 3 wt.% H_2O_2 aqueous solution was added dropwise under continuous stirring until gelation was observed. After being stirred for at least 30 min, the gel suspension was transferred into a 50 mL glass beaker and placed in an oven for 3 days at 40 ºC to slowly evaporate the solvent under static conditions. The final mesoporous product was collected after several

washing cycles (one cycle with 20 mL ethanol and three cycles with 20 mL DI water), vacuum filtration and drying at 40 ^{o}C overnight.

3.1.3 Synthesis of MoS_2 NSs

For the synthesis of the MoS_2 NSs, monovacant Keggin-type phosphomolybdate ($Na_7[PMo_{11}O_{39}]$) was synthesized following a previously reported procedure.[17] Next, 0.0175 mmol of $Na_7[PMo_{11}O_{39}]$ was dissolved in 10 mL of deionized water under stirring at RT. Then, 1 mmol of thioacetamide (CH_3CSNH_2) was added and the resulting mixture was kept under stirring for 2 h at RT. The final blue solution was placed in a 30 ml Teflon-lined autoclave and heated in an oven at 200 ^{o}C for 12 h. The black precipitate was collected by centrifugation, washed with water and dried at 60 ^{o}C for 24 h.

For comparison purpose, MoS_2 microflakes were also prepared following a similar procedure, but using 0.0275 mmol of $(NH_4)_6Mo_7O_{24}{\cdot}4H_2O$ as Mo source.

3.1.4 Preparation of mesoporous MoS_2/CdS NCAs

Mesoporous networks of MoS_2 NSs and CdS NCs with different MoS_2 content, namely, 5, 10, 15, 20 and 25 wt.%, were prepared by a facile deposition method. For a typical synthesis of 20 wt.% MoS_2-modified CdS sample, 20 mg of the prepared MoS_2 NSs were added to a H_2O:isopropanol (IPA) solution (2:1 v/v, 30 mL) in a 50-mL beaker. The mixture was sonicated for 2 h until a homogeneous black suspension of MoS_2 NSs was formed. In a separate vial, 80 mg of the mesoporous CdS NCAs were dispersed in a H_2O:IPA solution (2:1 v/v, 5 mL) under vigorous stirring at RT. Finally, the suspension of MoS_2 NSs was added gradually to the CdS NCAs dispersion and the resulting green mixture was left under stirring and low heat (50–60 ^{o}C) for slow evaporation of the solvents. The respective 5, 10, 15 and 25 wt.% MoS_2-loading CdS

samples were prepared following the same procedure, by using the stoichiometric amount of MoS_2 NSs for each case.

A bulk-like MoS_2-modified CdS catalyst (designated as 20-MoS_2/CdS_*b*) was also prepared by depositing 20 wt.% of MoS_2 microflakes on the surface of mesoporous CdS NCAs.

3.2 Physical Characterization

X-Ray Diffraction Patterns of the MoS_2/CdS composites were collected using a Panalytical X'pert Pro MPD System with Cu Kα (λ= 1.5418 Å) radiation, operated at 45kV and 40mA. Elemental microprobe analyses were conducted on JEOL JSM-6390 LV scanning electron microscope (SEM) equipped with an Oxford INCA PentaFETx3 energy-dispersive X-ray spectroscopy (EDS) detector (Oxfordshire, UK). For EDS analysis, due to the overlap of Mo-Lα and S-Kα lines, the samples were annealed at 800 ^oC for 3 h in order to detect only the Mo:Cd atomic ratio. All the measurement was performed on at least five different regions of each sample using 20 kV accelerating voltage and 60 s accumulation time. Transmission electron microscopy images were collected on a JEOL JEM-2100 instrument (LaB_6 filament) operated at 200 kV and the samples were prepared by dispersing fine powders in ethanol using sonication and then drop-casting on a holey carbon-coated Cu grid. The chemical state of elements was examined using X-ray photoelectron spectroscopy (XPS) analysis conducted on a SPECS spectrometer using a Phoibos 100 1D-DLD electron analyzer and a Al Kα radiation as the energy source (1486.6 eV). Binding energy values were corrected for charging by assigning a bending energy of 284.8 eV to the C 1s signal of adventitious carbon. UV-vis/near IR diffusion reflectance spectra were recorded on a Shimadzu UV-2600 optical spectrophotometer using $BaSO_4$ powder as a 100% reflectance reference.

The absorption spectra were converted from diffuse reflectance data using the Kubelka-Munk function: $\alpha/S = (1–R)^2/(2R)$, where R is the measured reflectance and α, S are the absorption and scattering coefficients, respectively. Specific surface areas and pore sizes were obtained from N_2 adsorption-desorption isotherms at –196 ^oC using a Quantachrome NOVA 3200*e* analyzer. Before each measurement, the samples were outgassed at 80 ^oC under vacuum ($<10^{-5}$ Torr). The specific surface areas were calculated from the adsorption data (P/P_o range 0.04–0.22) using the Brunauer-Emmett-Teller (BET) method, and the total pore volumes were estimated from the amount of adsorbed N_2 at P/P_o=0.98. The pore size distributions were derived from the absorption isotherms using the non-local density functional theory (NLDFT) method. Time-resolved photoluminescence spectroscopy was performed at room temperature using an Edinburgh instruments FS5 spectrofluorometer equipped with a 375 laser as light source.

3.3 Electrochemical measurements

Mott-Schottky, Nyquist plots and current-voltage (J–V) curves were measured in a 0.5 M Na_2SO_4 electrolyte (pH=7) using a single-channel potentiostat/Galvanostat system (Princeton Applied Research VersaSTAT 4) equipped with a standard three-electrode cell, consisting of a sample-coated FTO working electrode, an Ag/AgCl (saturated KCl) reference electrode, and a Pt-wire counter electrode. The working electrodes were prepared as follows: 10 mg of each sample were dispersed in 1 mL of 2-propanol and DI water solution (1:2 v/v). Then, 20 μL of Nafion aqueous solution (5 wt.%) were added and the mixtures were sonicated for 15 min and left under vigorous stirring for 24 h. When a uniform suspension was formed, 100 μL of each sample were dropped

onto a fluorine-doped tin oxide (FTO, 10 Ω/sq) glass substrate (effective surface 1 x 1 cm^2) and the films were dried under low heat (40–50 ^oC) for ca. 1 h.

The space-charge capacitance (C_{sc}) of the semiconductor/electrolyte interface was obtained at 1 kHz, with 10 mV AC voltage amplitude and the measured flat-band potentials were converted to the normal hydrogen electrode (NHE) scale using the equation: $E_{NHE} = E_{Ag/AgCl} + 0.197$, where E_{NHE} is the potential with respect to NHE and $E_{Ag/AgCl}$ is the measured potential with reference to the Ag/AgCl scale.

The donor density (N_D) of the as-prepared materials was calculated according to the Mott-Schottky equation: $N_D = C_{sc}^2 \cdot 2 \cdot (E – E_{FB}) / \varepsilon \cdot \varepsilon_0 \cdot e_0$, where, C_{SC} is the space charge capacitance, E is the applied potential, E_{FB} is the flat band potential, N_D is the donor density of electrode material, ε is the relative dielectric constant (8.9 for CdS), ε_0 is the vacuum permittivity (8.8542×10^{-14} F cm^{-1}), e_0 is the elementary charge (1.602×10^{-19} C) and the term $(E - E_{FB}) \cdot C_{SC}^2$ is the reciprocal of the slope of the Mott-Schottky plot.

For Nyquist plots, the different current output was measured throughout a frequency range of 1 Hz to 1 MHz using a small AC perturbation of 10 mV, under open-circuit potential conditions. The electrochemical impedance data were fitted to an equivalent circuit model using ZView Software.

3.4 Photocatalytic water splitting study

The photocatalytic H_2 evolution experiments were performed in an airtight Pyrex glass reactor containing 20 mg of the catalyst in 20 ml aqueous solution with Na_2S (0.35 M) and Na_2SO_3 (0.25 M) as sacrificial reagents. A 300 W xenon lamp (Variac Cermax) with a UV-cutoff filter (>420 nm) was used as a visible light source. Before irradiation, the reaction mixture was held under anaerobic conditions with argon (Ar) purging for 30 min. During the experiment, 100 μL of gas was collected from the reactor's

headspace and the generated H_2 was analyzed using gas chromatography (Shimadzu GC-2014, TCD, with Ar as the carrier gas). The temperature of the reaction solution was maintained at 20 ± 2 ^{o}C by a water-cooling system.

The apparent quantum efficiency (AQE) was estimated by measuring the amount of hydrogen evolved at a λ = 420 ± 10 nm irradiation wavelength, using the following equation:

AQE = (number of evolved hydrogen molecules x 2) / (number of incident photons).

The energy of photons was determined using a StarLite power meter equipped with a FL400A-BB-50 thermal sensor (Ophir Optronics Ltd).

4. Results and Discussion

4.1 Synthesis and structural characterization of MoS_2/CdS catalysts

Porous networks of connected CdS NCs and 2H-MoS_2 NSs were produced using a polymer-templated oxidative aggregating method followed by a wet-chemical deposition process. Initially, 2D nanolayers of MoS_2 were prepared thought a hydrothermal sulfurization reaction, using $Na_7[PMo_{11}O_{39}]$ and thioacetamide as Mo and S source, respectively.[18] Upon heating to a certain temperature, thioacetamide begins to decompose and liberate H_2S gas that is capable of transforming MoO_x^{n-} species into MoS_2. The X-ray diffraction (XRD) pattern of the as-made MoS_2 NSs, in Figure **7**, indicates the successful chemical transformation of phosphomolybdate clusters into MoS_2 under our liquid-phase conditions. All the diffraction peaks can be assigned to the hexagonal (2H) phase of MoS_2. Besides, the broadened XRD diffractions point to the nanoscale dimension of MoS_2 layers.

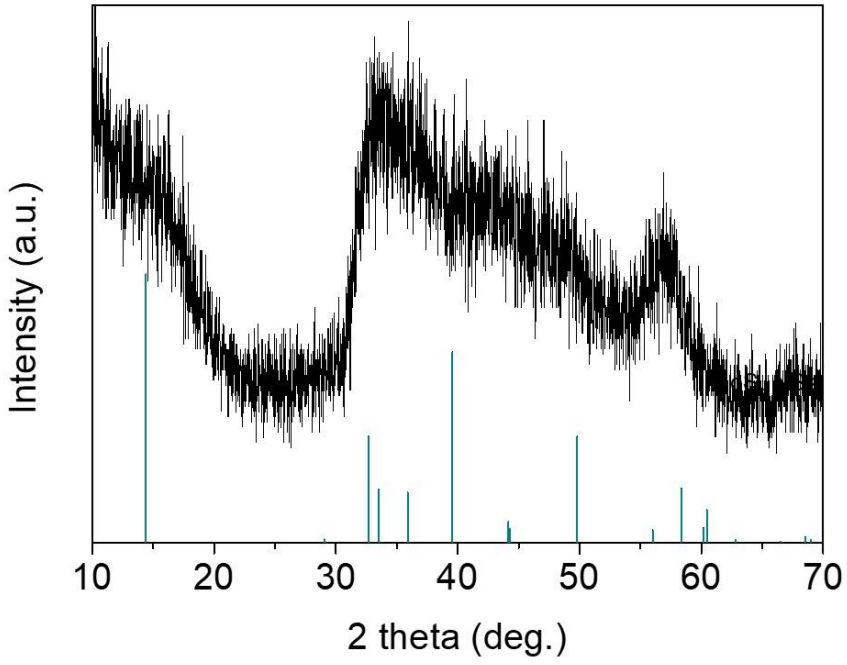

Figure 7. XRD pattern of the MoS_2 NSs. The XRD pattern shows diffraction peaks that corresponds to the hexagonal (2H) phase of MoS_2 (JCPDS card no. 77-1716).

Next, a porous network of CdS NC assemblies (NCAs) was synthesized by an oxidative cross-linking polymerization of thiol-capped CdS nanoparticles in the presence of a tri-block copolymer (Pluronic F-127) template. The MoS_2-modified mesoporous networks of CdS where then obtained by a deposition method where the liquid exfoliated MoS_2 NSs are incorporated onto the surface of CdS NCAs. Following this method, a series of *n*-MoS_2/CdS NCAs catalysts were prepared with various loadings of MoS_2, namely, *n* = 5, 10, 15, 20 and 25 wt.%. The Mo/Cd atomic ratios of the as-prepared samples were determined by energy dispersive X-ray spectroscopy (EDS). All the EDS spectra in Figure **8** affirm that the Mo content in MoS_2/CdS NCAs is very close to the nominal composition of the catalysts (within a 8% deviation), indicating complete deposition of MoS_2 on the CdS surface.

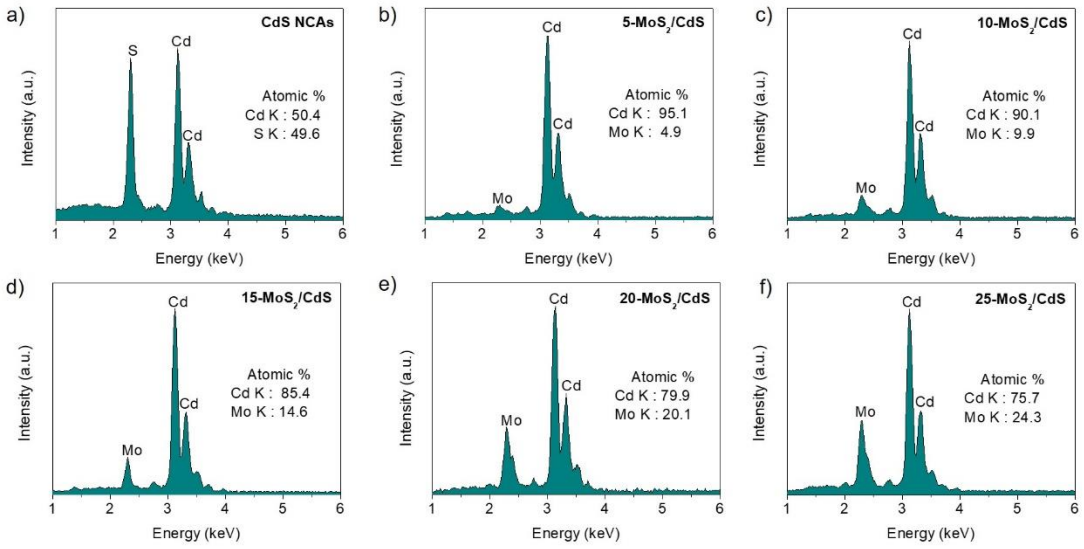

Figure 8. Typical EDS spectra of the mesoporous CdS and *n*-MoS_2/CdS NCAs.

The crystallinity and surface chemistry of the as-synthesized materials were examined via X-ray diffraction (XRD) and X-ray photoelectron spectroscopy (XPS). As can be seen from Figure **9,** all the XRD patterns of CdS and MoS_2/CdS NCAs display three distinct diffraction peaks at scattering angles of $2\theta = 20^o–60^o$, which can

be indexed to the (111), (220) and (311) reflections of the CdS zinc-blende structure (JCPDS card no. 42-1411).

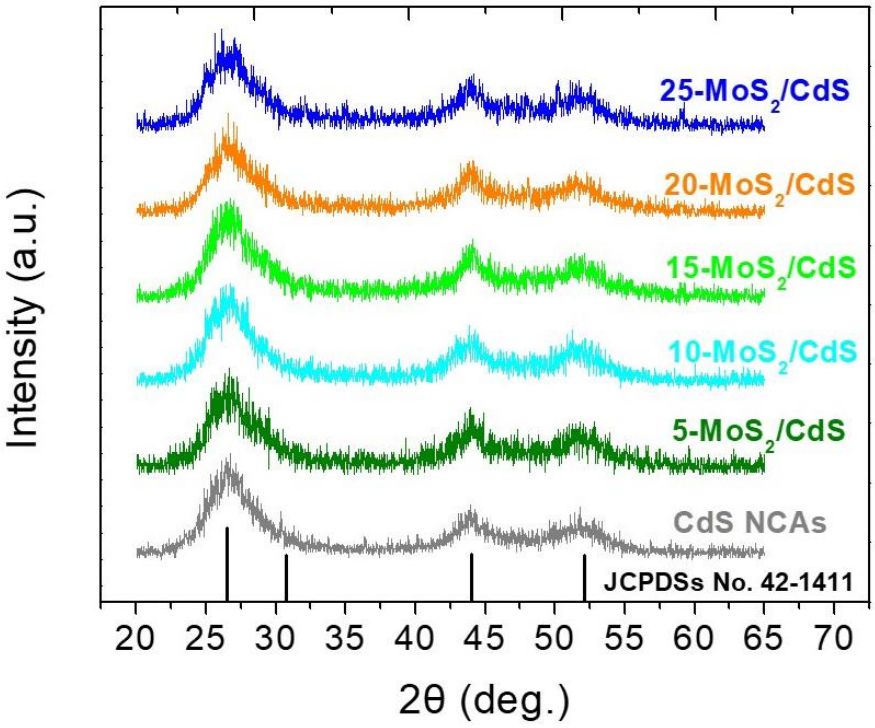

Figure 9. XRD patterns of the mesoporous CdS and MoS_2/CdS NCAs. The standard diffraction lines of zinc-blende CdS according to the JCPDS card no. 42-1411 are also given (black lines).

Figure **10** displays typical XPS spectra of the mesoporous 20-MoS_2/CdS sample, which is the most active catalyst in this series. The XPS Cd 3d spectrum, in Figure **10a**, presents a prominent doublet peak at 405.3 and 412.2 ± 0.2 eV binding energies, corresponding to the Cd $3d_{5/2}$ and Cd $3d_{3/2}$ core level components of Cd^{2+} in CdS, respectively.[19] The XPS spectrum of the Mo 3d scan confirmed the presence of Mo^{4+} species in MoS_2, showing two peaks at 229.1 ± 0.2 eV ($3d_{5/2}$) and 232.4 ± 0.2 eV ($3d_{3/2}$) binding energies with a spin-obit splitting of 3.3 eV (Figure **10b**).[20] Besides the characteristic Mo^{4+} 3d signal, there exists a weak doublet peak at relatively higher binding energy (231 ± 0.2 eV and 234.4 ± 0.2 eV), which can be referred to unsaturated Mo^{4+} atoms and/or higher oxidation state of Mo^{5+} species due to the inadequate surface

oxidation after the synthesis process.[21] As for the singlet peak observed at 226.6 ± 0.2 eV is attributed to the S 2s line of sulfides (S^{2-}).[22] Furthermore, the XPS S 2p spectrum (Figure **10c**) exhibited a prominent peak at 162.2 ± 0.3 eV that is characteristic of the S^{2-} ions in metal sulfides.[23] Quantitative analysis of the XPS spectra also indicated a Mo-to-Cd atomic ratio close to 20.4:79.6 that corresponds to the ~22.1 wt.% of MoS_2 content, in agreement with the EDS results.

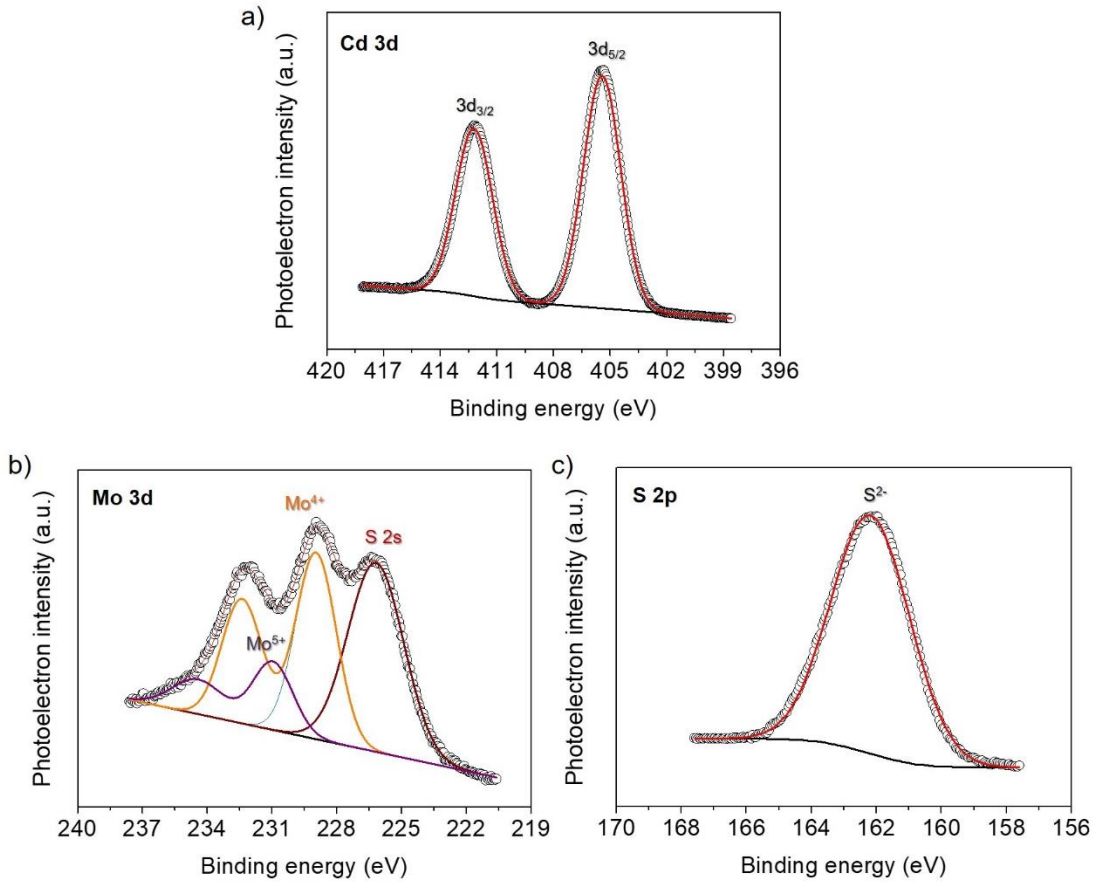

Figure 10. Typical XPS core-level spectra of the Cd 3d (a), Mo 3d (b) and S 2p (c) region for the 20-MoS_2/CdS catalyst.

The morphology of the MoS_2-modified CdS NCAs was examined via transmission electron microscopy (TEM). Typical TEM images for the mesoporous MoS_2/CdS catalyst containing 20 wt.% MoS_2 (20-MoS_2/CdS) are shown in Figure **11**. The network structure in 20-MoS_2/CdS sample exhibits a composition of connected CdS nanoparticles with an average diameter of ~4–5 nm (Figure **11a**). Furthermore, from

the high-resolution TEM (HRTEM) investigation in Figure **11b**, some layered particles (appeared as dark spots) with a lateral dimension of about 10–15 nm can be seen on the surface of CdS. A careful examination of these layered materials reveals an interlayer distance of ~6.5 Å that reasonably correlates to the (002) planes of MoS_2 NSs. This suggests a small enlargement of the interlayer spacing of MoS_2 NSs relative to the bulk MoS_2 (6.2 Å), possibly due to the small particle size. Based on the above results, MoS_2 NSs are deposited on the surface of CdS and, more importantly, with intimate contact, which is beneficial for the interfacial charge transfer within the heterostructured catalyst.

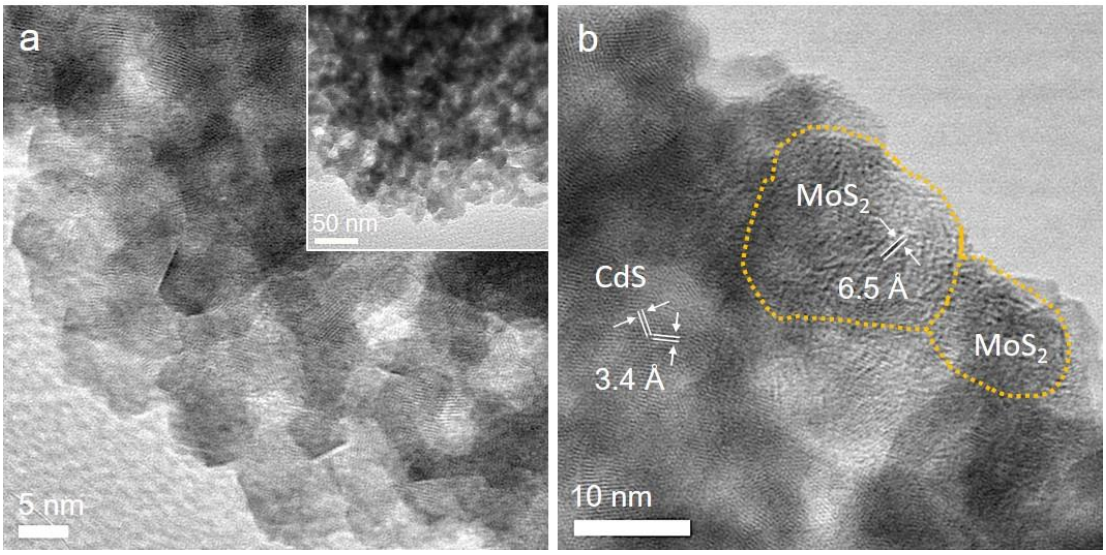

Figure 11. Typical TEM images of the 20-MoS_2/CdS NCAs catalyst. In panel b, the lattice fringes of the (002) CdS planes (3.4 Å) and the interlayer spacing of the MoS_2 (6.5 Å) can be seen.

The porosity of the as-synthesized materials was probed with N_2 physisorption measurements at –196 ^oC. The N_2 adsorption-desorption isotherms and the corresponding pore size distribution plots of mesoporous CdS and 20-MoS_2/CdS NCAs are demonstrated in Figure **12**. The respective plots for the other MoS_2-modified materials (that is, with 5, 10, 15 and 25 wt.% MoS_2 content) are depicted in Figure **13**. All samples exhibit typical type-IV isotherms with a H_2-type hysteresis loop (according

to International Union of Pure and Applied Chemistry classification), suggesting mesoporous structures with interconnected pores.[24]

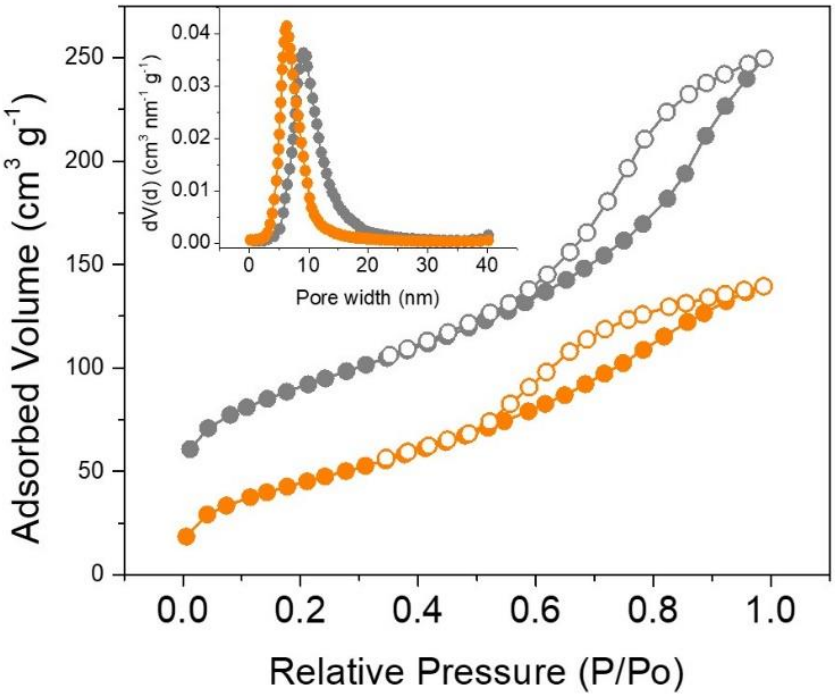

Figure 12. N_2 adsorption and desorption isotherms at −196 °C for the mesoporous CdS (gray symbols) and 20-MoS_2/CdS (orange symbols) NCAs. The N_2 isotherms of CdS NCAs are offset by 30 cm^3 g^{-1} for clarity. Inset: the corresponding NLDFT pore size distributions derived from the adsorption branch of isotherms.

The mesoporous MoS_2/CdS NCAs possess a Brunauer-Emmett-Teller (BET) surface area of 159–196 m^2 g^{-1} and a total pore volume of 0.20–0.26 cm^3 g^{-1}, which are slightly lower than those of the pristine CdS sample (225 m^2 g^{-1} and 0.28 cm^3 g^{-1}, respectively). The pore size in the prepared materials was assessed from the adsorption branch of isotherms using the non-local density functional theory (NLDFT) fitting model.[25] The results reveal that all the samples possess a quite narrow pore size distribution with an average pore size of ~9.1 nm for CdS NCAs and ~6.1–8.1 nm for the MoS_2-modified catalysts (insets of Figures **12** and **13**). The slight decrease in porosity of composite materials with increasing MoS_2 content can be explained by the successful deposition

of MoS_2 NSs on the pore walls of mesoporous CdS, which is consistent with our TEM observations. The textural parameters for all the prepared materials are summarized in Table **1**.

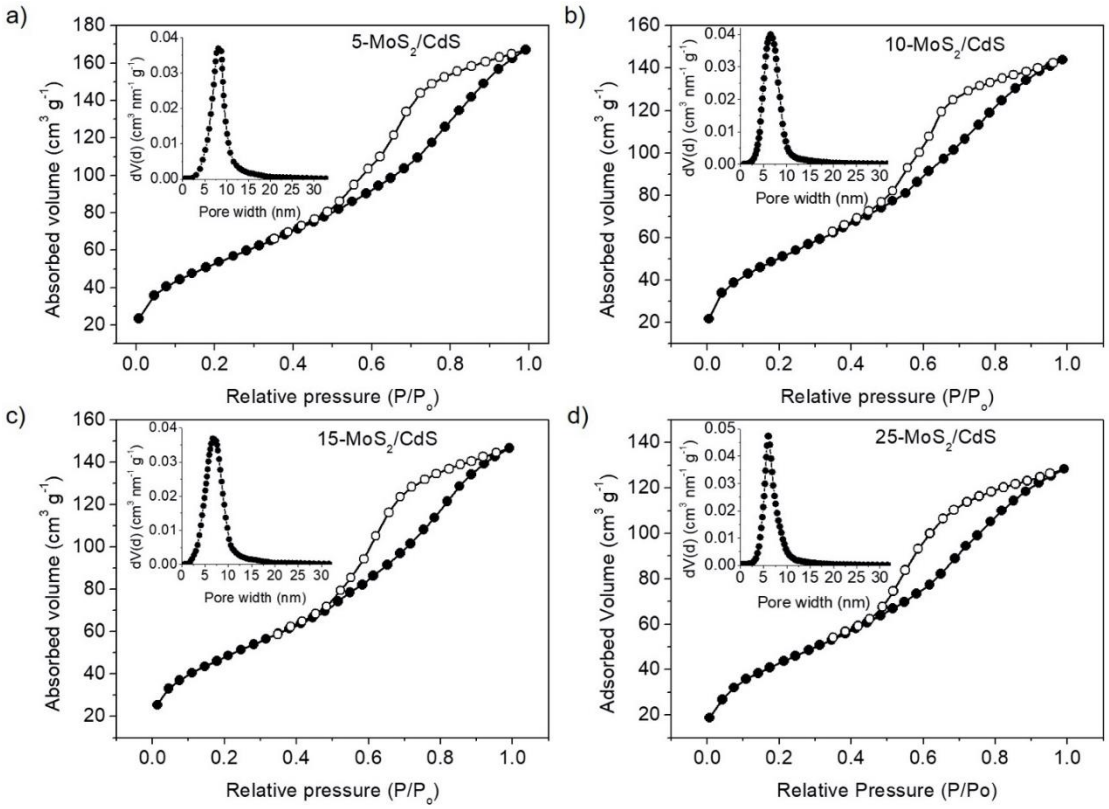

Figure 13. N_2 adsorption (filled cycles) and desorption (open cycles) isotherms at –196 ^oC for the mesoporous (a) 5-MoS_2/CdS, (b)10-MoS_2/CdS, (c) 15-MoS_2/CdS and (d) 25-MoS_2/CdS NCAs. Insets: The corresponding NLDFT pore size distributions calculated from the adsorption branch of isotherms.

To determine the optical absorption properties of CdS and MoS_2/CdS NCAs, ultraviolet–visible/near-IR (UV–vis/NIR) diffuse reflectance spectroscopy was performed. As shown in Figure **14a**, the mesoporous CdS NCAs show an intense optical absorption onset at ~457 nm (2.71 eV), which is attributed to the intrinsic electron transition from the valence band (VB) to the conduction band (CB) in CdS. Notably, CdS NCAs exhibit a remarkable blue shift in absorption onset compared to the bulk

CdS (it has a bandgap of 2.4 eV) due to the quantum confinement effect arising from the very small size of the constituent CdS NCs (ca. 4–5 nm in diameter according to TEM observations). Meanwhile, as compared to CdS, the MoS_2-modified materials show a small red shift of the absorption edge. Specifically, the optical bandgap (E_g) of the MoS_2/CdS catalysts estimated from Tauc plots [$(\alpha hv)^2 \propto (hv - E_g)$, where, α is the absorption coefficient and hv is the energy of incident photons] falls in the range of 2.63 to 2.71 eV (inset of Figure **14a**). This tiny, yet noteworthy, red shift in energy gap suggests strong interactions between CdS and MoS_2, which allows facile electronic transport across the interface to develop.

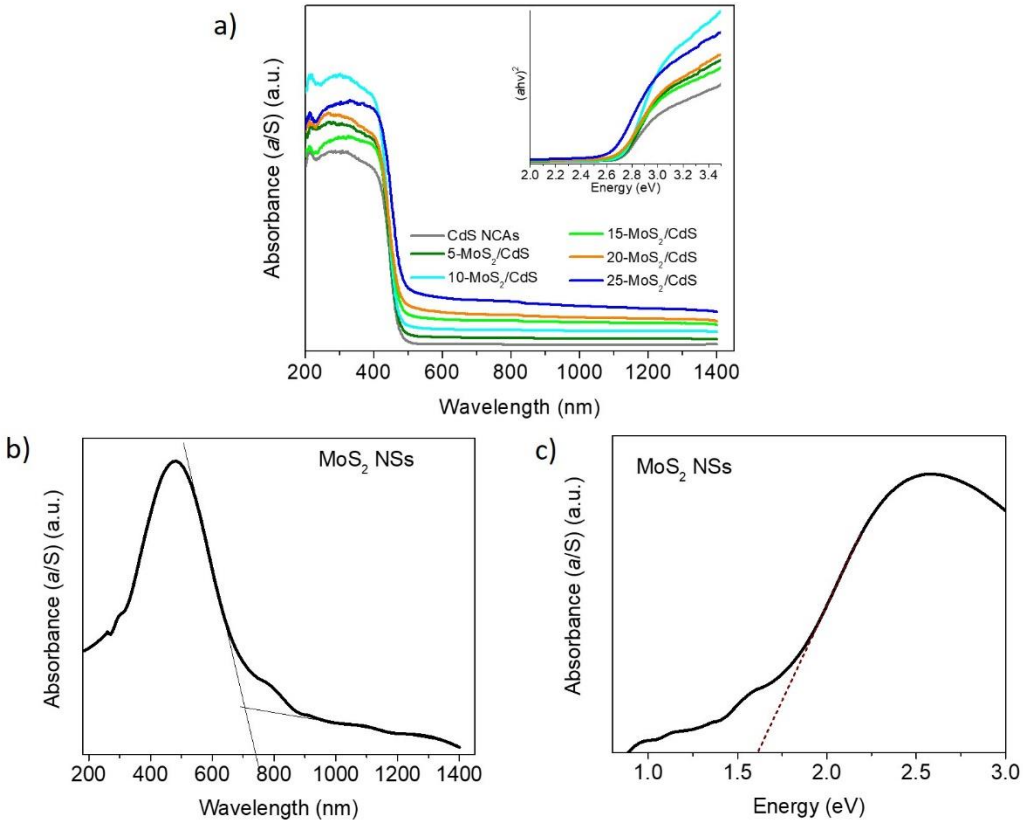

Figure 14. (a) Optical absorption spectra of mesoporous CdS and MoS_2/CdS NCAs with 5, 10, 15, 20 and 25 wt.% MoS_2 content. Inset: the corresponding Tauc plots for direct bandgap semiconductors. (b) Optical absorption spectrum and (c) the corresponding absorbance vs energy plot of the as-synthesized MoS_2 NSs.

Furthermore, the UV–vis/NIR spectra of MoS_2-modified materials also show an absorption tail of 480–1400 nm, which can be related to the visible and NIR light response of MoS_2 NSs. Indeed, the intensity of this absorption tail progressively increases with increasing the MoS_2 content in the MoS_2/CdS samples and also correlates well with the absorption spectrum of MoS_2 NSs (Figure **14b** and **14c)**. The UV–vis/NIR spectrum of MoS_2 NSs indicated an energy bandgap of 1.62 eV, which is greater than the typical bandgap of bulk MoS_2 (~1.3 eV), probably due to the small size and few-layered structure of the as-synthesized MoS_2 NSs.

Table 1. Chemical composition and textural and optical properties of the as-prepared CdS and MoS_2/CdS NCAs.

Catalyst	**MoS_2 content[†] (wt.%)**	**BET surface area ($m^2\ g^{-1}$)**	**Pore volume ($cm^3\ g^{-1}$)**	**Pore size (nm)**	**Energy gap (eV)**
CdS NCAs	-	225	0.34	9.1	2.71
5-MoS_2/CdS	5.4	196	0.26	8.1	2.71
10-MoS_2/CdS	10.8	185	0.23	6.6	2.71
15-MoS_2/CdS	15.9	176	0.23	6.6	2.68
20-MoS_2/CdS	21.7	166	0.22	6.6	2.68
25-MoS_2/CdS	26.2	159	0.20	6.1	2.63
20-MoS_2/CdS_*b*	21.5	169	0.23	7.6	2.67

[†]Based on EDS analysis.

4.2 Photocatalytic water reduction study

The photocatalytic reaction experiments of the MoS_2/CdS catalysts were carried out under visible light irradiation ($\lambda > 420$ nm) using Na_2SO_3/Na_2S aqueous solution as sacrificial reagents. In Figure **15a,** a linear increase of H_2 evolution rate is observed for all the photocatalysts, which implies that they exhibit excellent H_2-evolution activity. To further compare the photocatalytic H_2 production over the various photocatalysts, the average rates of hydrogen evolution were determined. As shown in Figure **15b** the photocatalytic activity of the MoS_2/CdS composites is about 4–6 times higher than that of the pure mesoporous CdS NCAs. It is also demonstrated that H_2 evolution rate increases with increasing the MoS_2 loading content on the CdS surface and reaches a maximum (0.38 mmol h^{-1}) at 20 wt.%.

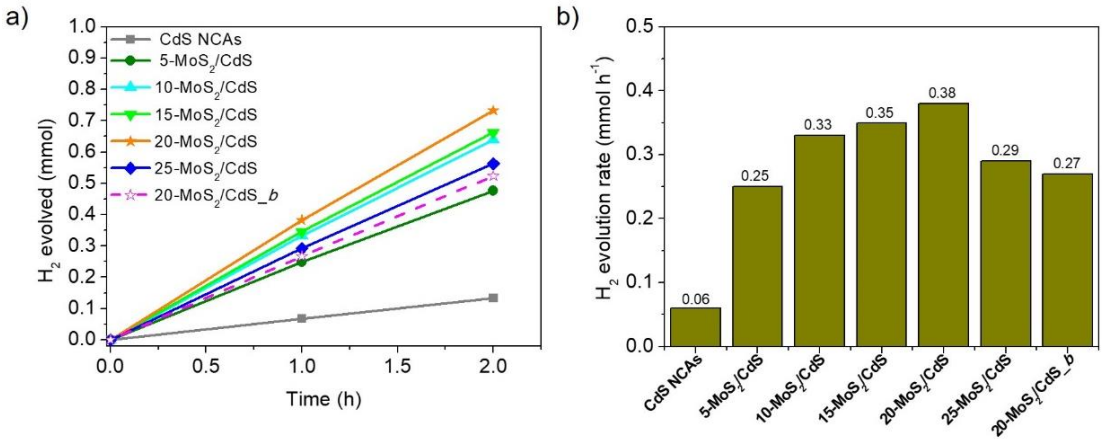

Figure 15. (a) Time courses of photocatalytic H_2 evolution, and (b) H_2-evolution rates for the mesoporous CdS and *n*-MoS_2/CdS NCAs. The H_2-evolution results for the catalyst with 20 wt.% bulk MoS_2 (20-MoS_2/CdS_*b*) are also given. The photocatalytic reactions were performed as follows: 20 mg of catalyst were dispersed in 20 mL aqueous solution containing 0.35 M Na_2S and 0.25 M Na_2SO_3; 300-W Xenon light radiation with a long-pass cut-off filter ($\lambda \geq 420$ nm), 20 ±2 ^oC.

This indicates that deposition of MoS_2 NSs on the surface of mesoporous CdS plays an important role in enhancing the photocatalytic performance. However, further increase of the MoS_2 loading content (25 wt.%) can cause light shading effect on CdS

nanoparticles and/or the formation of interfacial charge-carrier recombination centers, leading to a decrease in the H_2-production rate (0.29 mmol h^{-1}).

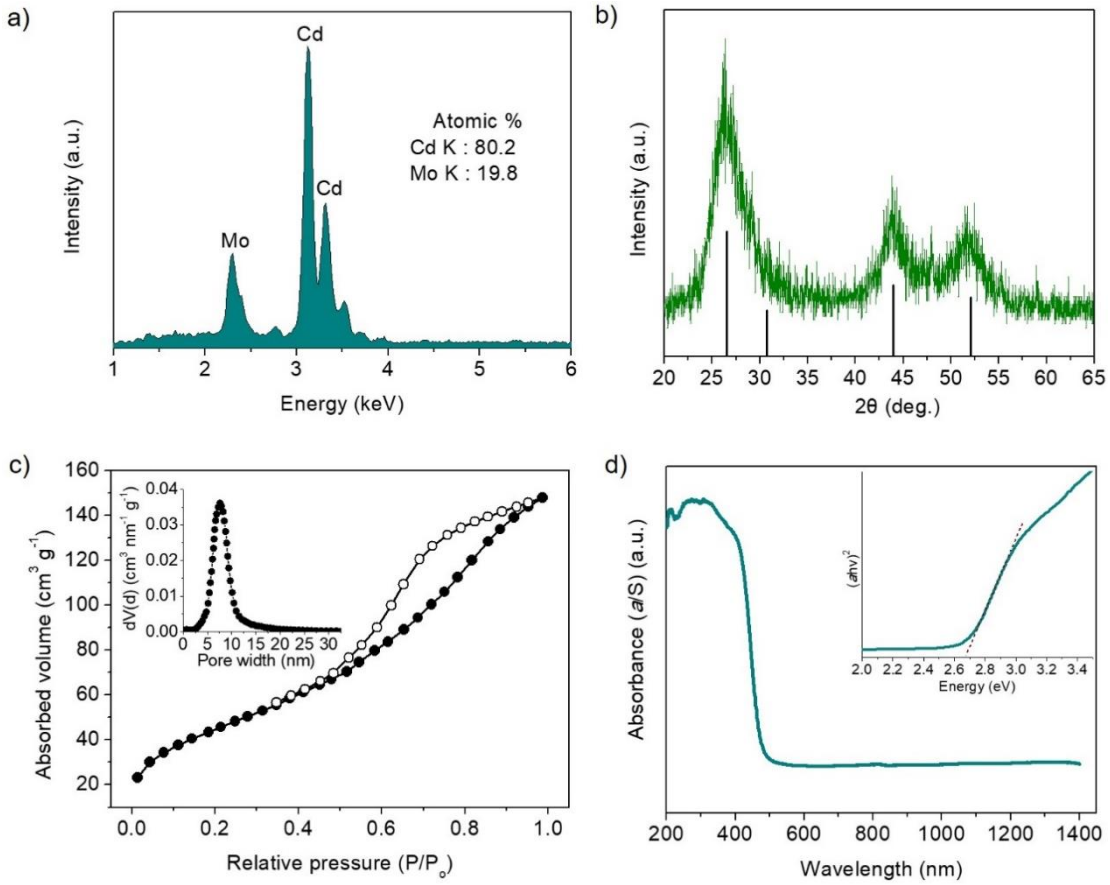

Figure 16. (a) Typical EDS spectrum, (b) XRD pattern showing also the standard diffraction lines of zinc-blende CdS according to the JCPDS card No.42-1411, (c) Nitrogen adsorption-desorption isotherms at –196 °C and the corresponding NLDFT pore-size distribution plot (inset), and (d) optical absorption spectrum and Tauc plot (inset) of the mesoporous 20-MoS_2/CdS_*b* sample.

To elucidate the morphological effect, a bulk MoS_2-modified CdS mesoporous heterostructure was prepared by depositing 20 wt.% of MoS_2 microflakes on the surface of mesoporous CdS NCAs (indicated as 20-MoS2/CdS_*b*). Its H_2 evolution performance was examined under identical conditions (i.e., using 20 mg of 20-MoS_2/CdS_*b* in 20 mL of 0.35 M Na_2S/0.25 M Na_2SO_3 aqueous solution; $\lambda \geq 420$ nm light radiation, 20 ± 2 °C). EDS analysis revealed that this catalyst contains 21.5 wt.%

of MoS_2 (Figure **16a**). Also, it possesses almost identical textural and optical characteristics with those of the nano-heterostructured 20-MoS_2/CdS analogue, as inferred by XRD, N_2 physisorption and UV–vis/NIR measurements (Figures **16b-d**), see Table **1**. Interestingly, the reference 20-MoS_2/CdS_*b* catalyst exhibited about 1.4-times lower H_2-evolution performance (0.27 mmol h^{-1}) compared to 20-MoS_2/CdS, even though having similar composition, optical absorption and porosity (Figures **15a** and **b**). Therefore, it is concluded that the pronounced enhancement in H_2 production activity of the MoS_2/CdS nanojunction networks is related to the nanoscale size of the MoS_2 layers, which probably contributes to the increase concentration of active MoS_2 edge-sites and better electronic communication with the CdS host material. This assertion is further supported by photoluminescence and electrochemical studies (see below).

To further optimize the reaction conditions, a series of photocatalytic H_2 evolution tests were performed using different sacrificial hole scavengers and mass loadings of the 20-MoS_2/CdS catalyst. As shown in Figure **17**, a series of sacrificial reagents (i.e., phenol (PhOH, 0.35 M), methanol (MeOH, 10% v/v), triethanolamine (TEOA, 10% v/v), triethylamine (TEA, 10% v/v), lactic acid (LA, 10% v/v) and Na_2S/Na_2SO_3 (0.35 M/0.25 M)) was examined to evaluate the photocatalytic behavior of 20-MoS_2/CdS for H_2 evolution. As indicated in Figure **17**, optimal results were obtained with S^{2-}/SO^{3-} mixture and this sacrificial reagent was used during further studies. In general, S^{2-} and SO^{3-} ions not only promote H_2 generation by consuming the surface-reaching holes, but also prevent sulfur-containing catalysts from photocorrosion by replenishing sulfur lattice defects originated from anodic photocorrosion.[26]

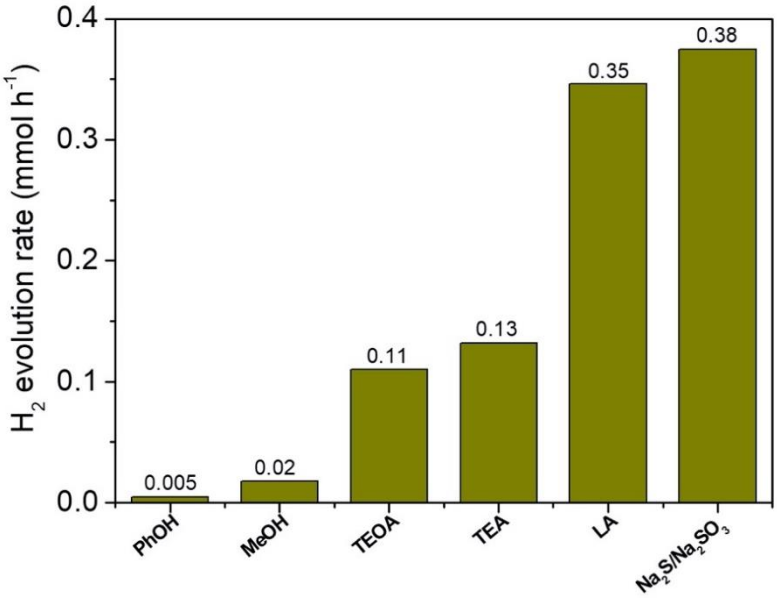

Figure 17. Photocatalytic H_2 evolution rates for the mesoporous 20-MoS_2/CdS catalyst using different sacrificial reagents: phenol (PhOH, 0.35 M), methanol (MeOH, 10% v/v), triethanolamine (TEOA, 10% v/v), triethylamine (TEA, 10% v/v), lactic acid (LA, 10% v/v) and Na_2S/Na_2SO_3 (0.35 M/0.25 M) aqueous solution. All photocatalytic reactions were performed as follows: 20 mg of catalyst dispersed in a 20 mL aqueous solution containing the sacrificial reagent; 300-W Xe light radiation with a long-pass cut-off filter allowing $\lambda \geq 420$ nm, 20 ±2 °C.

Moreover, photocatalytic results using different loadings of the 20-MoS_2/CdS catalyst indicated that the rate of H_2 generation increases with increasing catalyst's mass concentration and reaches a maximum at 1 g L^{-1} (Figure **18**). This increment in H_2-production activity is correlated with the increased light absorption by the catalyst's particles. As for the higher catalyst concentration (1.5 g L^{-1}), the slight reduction of the H_2 evolution rate (0.3 mmol h^{-1}) can be attributed to the light scattering from excessive particles. Overall, 20-MoS_2/CdS mesoporous catalyst under the optimum reaction conditions (1 g L^{-1} catalyst dose in Na_2S/Na_2SO_3 aqueous solution) achieves a H_2-evolution rate of almost 0.4 mmol h^{-1} (or ~19 mmol h^{-1} g^{-1} mass activity), and obtained an apparent quantum yield (AQY) of 51.2% at 420 ± 10 nm, assuming that all incident photons were absorbed by the catalyst particles. To the best of our knowledge, this

efficiency is the highest reported for MoS_2-modified CdS catalysts. A comparison of the photocatalytic H_2-evolution activities of various MoS_2/CdS composite catalysts is shown in Table **2.**

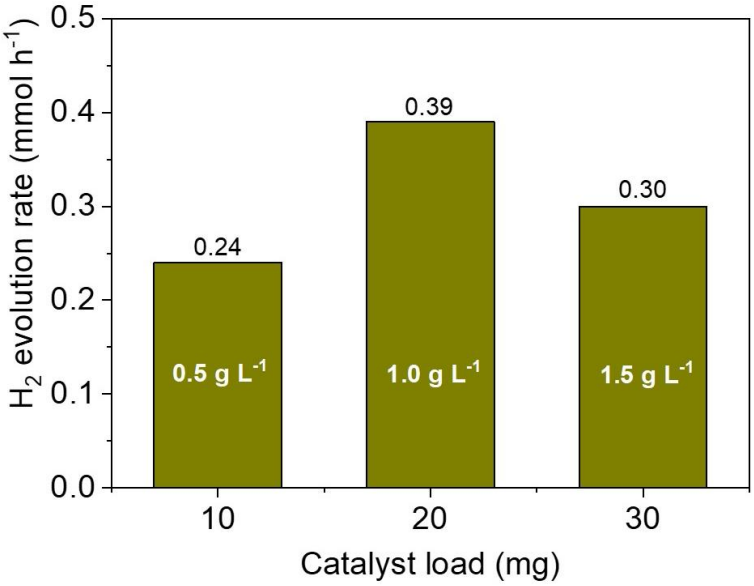

Figure 18. Photocatalytic H_2 evolution activities for different loadings of 20-MoS_2/CdS catalyst. Experimental conditions: 10–30 mg of catalyst, 20 mL aqueous solution containing 0.35 M Na_2S and 0.25 M Na_2SO_3, 300 W Xenon light radiation with a long-pass cut-off filter ($\lambda \geq 420$ nm), 20 ± 2 ^oC.

Table 2. Comparison of H_2-production activities for different reported MoS_2/CdS-based photocatalysts.

Photocatalyst	**Reaction Conditions**	**Light Source**	**H_2 evolution rate**		**Quantum Yield (QY)**	**Ref.**
			(µmol h^{-1})	**(µmol g^{-1} h^{-1})**		
0.2 wt.% MoS_2/CdS	100 mg catalyst, 10 % v/v lactic acid	300 W Xe lamp (λ≥420 nm)	540	5400	-	27
0.2 wt.% MoS_2 /CdS	100 mg catalyst, 10 % v/v lactic acid	300 W Xe lamp (λ≥420 nm)	533	5330	7.3% at 420 nm	28
0.9 mol% MoS_2/ CdS NPs	100 mg catalyst, 10 % v/v lactic acid	300 W Xe lamp (λ>420 nm)	1315	13150	-	29
6.9 wt.% feather-shaped MoS_2/CdS	50 mg catalyst, 0.5 M Na_2S, 0.5 M Na_2SO_3	300 W Xe lamp (λ≥400 nm)	192	3840	-	30

20 wt.% MoS_2 NSs/CdS NPs	20 mg catalyst, 10 % v/v lactic acid	300 W Xe lamp (λ≥400 nm)	137	6850	10.5% at 450 nm	31
15 wt.% MoS_2 /CdS NPs	80 mg catalyst, 0.1 M Na_2S, 0.02 M Na_2SO_3	300 W Xe lamp (λ≥400 nm)	382	4770	-	32
2 wt.% monolayer MoS_2/CdS	200 mg catalyst, 0.35 M Na_2S, 0.35 M Na_2SO_3	300 W Xe lamp (λ≥400 nm)	2100	10500	30.2% at 420 nm	33
	200 mg catalyst, 10 % v/v lactic acid		2590	12950	38.4% at 420 nm	
2 wt.% MoS_2/CdS microspheres	100 mg catalyst, 10 % v/v lactic acid	300 W Xe lamp (λ>400 nm)	406	4060	-	34
2.5 wt.% MoS_2 flowerlike/CdS nanorods	50 mg catalyst, 10 % v/v lactic acid	300 W Xe lamp (λ>400 nm)	551	11026	31.8% at 420 nm	35
20 wt.% 2D MoS_2/0D CdS	50 mg catalyst, 20 % v/v lactic acid	300 W Xe lamp (λ>400 nm)	84.8	1696	23.0% at 420 nm	36
10 wt.% MoS_2 NSs/CdS nanowires	20 mg catalyst, 20 % v/v lactic acid	300 W Xe lamp (λ≥400 nm)	1914	95700	46.9% at 420 nm	37
MoS_2/CdS NPs	60 mg catalyst, 10 % v/v lactic acid	300 W Xe lamp (λ≥420 nm)	314	5240	1.0% at 420 nm	38
10 wt.% MoS_2 NSs/CdS nanorods	200 mg catalyst, 10 % v/v lactic acid	300 W Xe lamp (λ≥420 nm)	9960	49800	41.4% at 420 nm	39
6.0 wt.% MoS_2 NSs/CdS nanorods	10 mg catalyst, 20 % v/v lactic acid	Natural solar irradiation	174	174000	-	40
1.0 wt.% MoS_2/CdS NSs	50 mg catalyst, 0.5 M Na_2S, 0.5 M Na_2SO_3	300 W Xe lamp (λ>400 nm)	87	1740	-	41
	50 mg catalyst, 20 % v/v lactic acid		436	8720		
MoS_2/CdS nanomaterials (molar ratio of Mo:Cd=1:6)	20 mg catalyst, 25 % v/v lactic acid	300 W Xe lamp (λ≥420 nm)	775	38750	14.7% at 420 nm	42
2 wt.% monolayer MoS_2/CdS	200 mg catalyst, 30 % v/v lactic acid, NaOH (pH~5)	300 W Xe lamp (λ≥420 nm)	1020	5100	-	43
CdS@MoS_2-5% irregular nanospheres	50 mg catalyst, 0.25 M Na_2S, 0.35 M Na_2SO_3	300 W Xe lamp (λ≥420 nm)	860	17203	24.2% at 420 nm	44
6.39 wt.% MoS_2/CdS NSs	100 mg catalyst, 0.35 M Na_2S, 0.25 M Na_2SO_3	300 W Xe lamp (λ≥420 nm)	3.7	370	0.65% at 420 nm	45
5 wt.% MoS_2 NSs/CdS particles	80 mg catalyst, 0.45 M Na_2S, 0.55 M Na_2SO_3	300 W Xe lamp (λ≥420 nm)	372	4650	7.3% at 420 nm	46

3 wt.% MoS_2/CdS hybrids	100 mg catalyst, 0.35 M Na_2S, 0.25 M Na_2SO_3	300 W Xe lamp (λ≥420 nm)	114	11400	1.2% at 420 nm	47
0.25 wt.% MoS_2 QDs/CdS	50 mg catalyst, 10 % v/v lactic acid	300 W Xe lamp (λ≥420 nm)	1032	206420	35.1% at 420 nm	48
	50 mg catalyst, 1.0 M $(NH_4)_2SO_3$		863	172600	29.3 % at 420 nm	
20 wt.% 1T MoS_2 NSs/CdS nanorods	10 mg catalyst, 10 % v/v lactic acid	500 W metal halide lamp (λ≥420 nm)	1324	132400	47.0% at 420 nm & 4.0% at 460 nm	49
5 at.% MoS_2/CdS	80 mg catalyst, 10 % v/v lactic acid	300 W Xe lamp (λ≥420 nm)	20	250	3.7% at 420 nm	50
3 wt.% 1T- MoS_2 QDs/CdS	2 mg catalyst, 10 % v/v lactic acid	500 W metal halide lamp (λ≥420 nm)	263	131700	50.4% at 420 nm	51
70 wt.% MoS_2 NSs/ CdS nanowires	50 mg catalyst, 10 % v/v triethanolamine	300 W Xe lamp	90	1790	-	52
7 wt.% 2D/2D MoS_2/CdS	10 mg catalyst, 10 % v/v lactic acid	300 W Xe lamp (λ≥420 nm)	184	18430	3.5% at 450 nm	53
20 wt.% MoS_2 NSs/CdS NCAs	**20 mg catalyst, 0.35 M Na_2S, 0.25 M Na_2SO_3**	**300 W Xe lamp (λ≥420 nm)**	**390**	**19500**	**51.2% at 420 nm**	**This work**

Apart from the high photocatalytic activity, the mesoporous 20-MoS_2/CdS NCAs also exhibited sufficient stability under the examined conditions. The stability of catalyst was examined by performing three consecutive 5-h photocatalytic runs. After each run, the catalyst was collected by centrifugation and re-dispersed in a fresh Na_2S/Na_2SO_3 aqueous solution. Before each photocatalytic reaction, the reaction cell was de-aerated by purging with Ar gas for 30 min until no H_2 and O_2 were detected by gas-chromatography (GC) analysis. As shown in Figure **19**, 20-MoS_2/CdS has a quite stable H_2-evolution rate, retaining almost 90% of its initial activity after 15 h of illumination. Nevertheless, a small decrease in H_2 evolution rate during the third cycle of reuse may hint some minor photocorrosion and/or catalyst mass loss during the recycling tests.

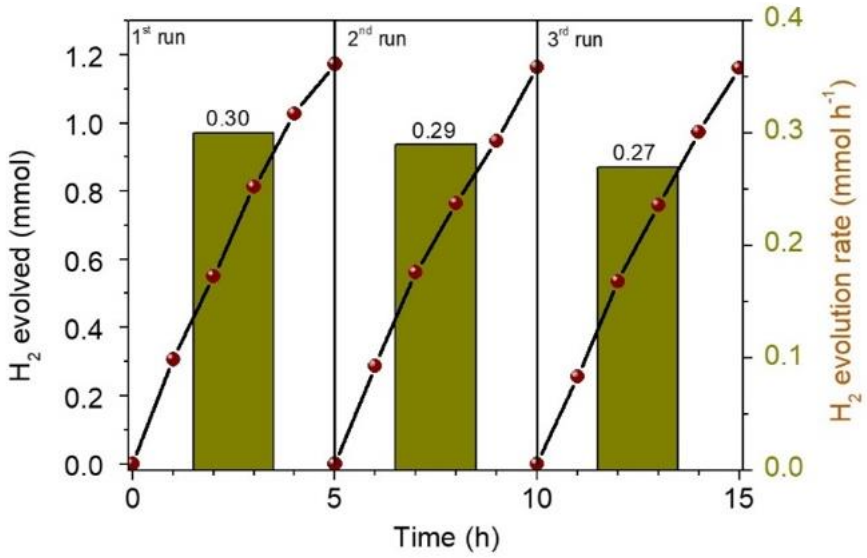

Figure 19. Photocatalytic recycling study of the 20-MoS_2/CdS catalyst. The columns show the H_2-evolution rates of the 5-h time intervals. The photocatalytic reactions were performed as follows: 20 mg of catalyst were dispersed in 20 mL aqueous solution containing 0.35 M Na_2S and 0.25 M Na_2SO_3; 300-W Xenon light radiation with a long-pass cut-off filter ($\lambda \geq 420$ nm), 20 ±2 ^oC.

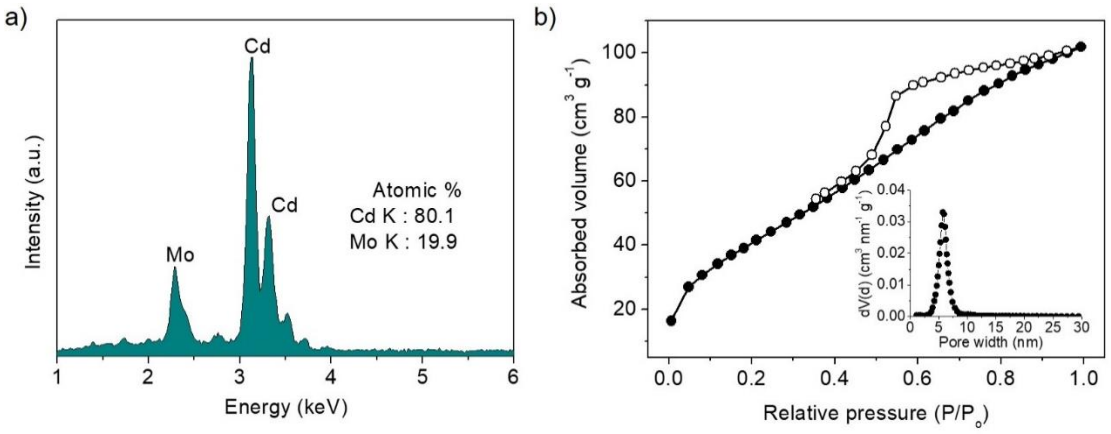

Figure 20. (a) Typical EDS spectrum and (b) N_2 adsorption-desorption isotherms at –196 ^oC and the corresponding NLDFT pore-size distribution (inset) for the 20-MoS_2/CdS catalyst retrieved after 15 h of photocatalytic reaction.

EDS, N_2 physisorption and XPS measurements were employed to assess the chemical and structural stability of the reused catalyst. The EDS spectra revealed a Mo/Cd atomic ratio of 19.9:80.1 that corresponds to a MoS_2 content of about 21.6 wt.%, while N_2 adsorption-desorption isotherms revealed a surface area of 156 $m^2\ g^{-1}$, pore volume of 0.16 $cm^3\ g^{-1}$ and pore size of ~6 nm (Figure **20**), which are very close to those of the fresh material. As shown by XPS spectra (see Figure **21**), no obvious change in surface chemical nature of the catalyst was observed after the recycling tests, proving the excellent stability of the 20-MoS_2/CdS NCAs under the examined conditions. Specifically, the Cd 3d XPS spectrum shows a doublet peak at 404.4 and 411.3 ± 0.2 eV, corresponding to the Cd $3d_{5/2}$ and Cd $3d_{3/2}$ core levels components of Cd^{2+} in CdS, respectively. The Mo 3d XPS spectrum shows two peaks at binding energies 229.3 and 232.5 ± 0.2 eV, which are assigned respectively to the $3d_{5/2}$ and $3d_{3/2}$ spin-orbit peaks of Mo^{4+} in MoS_2. The peak observed at 225.3 ± 0.2 eV is assigned to the S 2s line of sulfide (S^{2-}) ions. The S 2p XPS spectrum shows a broad signal at 161.5 ± 0.3 eV due to the S^{2-} ions. In addition, a small amount of sulfur species at certain higher oxidation states is, however, observed in the surface of CdS and MoS_2 NSs, deducing from the weak peak at 168.1 ± 0.3 eV.

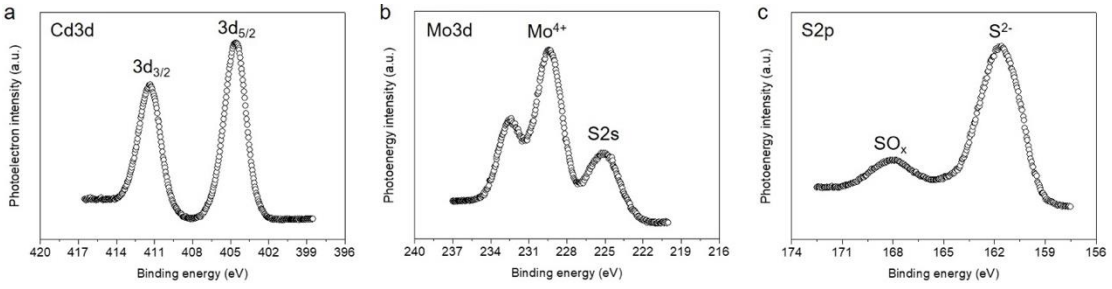

Figure 21. Typical XPS core-level spectra of the (a) Cd 3d, (b) Mo 3d and (c) S 2p region of the reused 20-MoS_2/CdS catalyst.

4.3 Role of MoS_2 in photocatalytic activity

In order to investigate the role of MoS_2 NSs in the catalytic activity and to better understand the charge-transfer dynamics at the nanoscale MoS_2/CdS interface, electrochemical impedance spectroscopy (EIS) was used. Figures **22a** and **23b** present the Mott-Schottky plots ($1/C_{SC}^2$ versus applied voltage E curves) of mesoporous CdS and MoS_2/CdS NCAs; all the examined materials were drop-casted as thin films on FTO substrates. As seen from the $1/C_{sc}^2$–E plots, all the samples display positive slopes indicating that electrons are the majority charge-carriers (n-type conductivity). Also from these plots, the flat band potentials (E_{FB}) of the samples were obtained using the tangent lines of the $1/C_{sc}^2$–E curves. As demonstrated in Table **3**, the determined E_{FB} potentials of MoS_2/CdS catalysts are –0.68 V to –0.75 V, whereas the E_{FB} position of CdS NCAs locates at –0.84 V; all electrochemical potentials are referred to the normal hydrogen electrode (NHE) at pH 7. By combining the flat-band potentials with the respective bandgaps (as obtained from optical UV-vis/NIR spectroscopy), the band-edge positions were calculated for each catalyst and the corresponding band diagrams are illustrated in Figure **22b**. More specifically, for the construction of band diagrams we assumed that the flat-band level lies very close to the CB edge for heavily doped n-type semiconductors (as inferred from Mott-Schottky measurements), and thus the valence band potential (E_{VB}) was calculated by adding the energy gap (E_g) to the E_{FB} level; the obtained E_{VB} values for each catalyst are also listed in Table **3**. As seen from the band diagrams, the E_{FB} level progressively undergoes an anodic shift, i.e., from –0.84 V to –0.68 V, with increasing the MoS_2 NSs content on the surface of CdS.

Moreover, as deduced from the slope of the $1/C_{SC}^2$ versus E lines, the amount of MoS_2 NSs also increases the donor density (N_D) of the MoS_2-modified CdS catalysts. The measured N_D values for the MoS_2/CdS samples range from 1.17 to 1.70×10^{17} cm^{-}

^{3}, which are significantly larger than that obtained for unmodified CdS NCAs (5.87 × 10^{16} cm^{-3}), as shown in Table **3**. The observed anodic shift in E_{FB} positions of MoS_2/CdS composites can be interpreted by the lower E_{FB} potential of MoS_2 NSs (i.e., –0.68 V vs NHE, as determined from Mott-Schottky analysis, see Figure **23a**) compared to that of CdS NCAs, which results to the formation of an internal electric field across the MoS_2/CdS junction (upon contact) that drives electrons from CdS to MoS_2 until the Fermi levels reach equilibrium. Such an electron transfer creates a depletion region at the CdS surface which lowers the CB energy potential closer to that of MoS_2, and this is consistent with the results of Figure **22b**. This intrinsic electric field at the junction interface is beneficial for photocatalysis because it improves the charge separation efficiency and thus increases the electron donor density (N_D) at the CdS CB, in line with the results in Table **3**.

Furthermore, the charge transfer properties of the prepared catalysts were also investigated by EIS Nyquist measurements. Figure **22c** presents the Nyquist plots of pristine and MoS_2-modified CdS samples measured in the 0.5 M Na_2SO_4 electrolyte at open circuit potential over a frequency span from 1 Hz to 1 MH. A typical Randles equivalent circuit was used to fit the experimental data consisted of a solution resistance (R_s), a double layer capacitance (C_{dl}), a charge-transfer resistance (R_{ct}) and a diffusional resistance element (Z_w), see inset of Figure **22c**, and the results of the fitting parameters are listed in Table **4**. The analysis indicated R_{ct} values for the MoS_2/CdS catalysts of ~2.7–6.3 kΩ, significantly lower than that of CdS NCAs (~13.5 kΩ) (Table **3**), suggesting a more favorable charge transfer across the MoS_2/CdS junction. Consequently, this process contributes to the enhanced catalytic efficiency of the MoS_2-modified CdS catalysts.

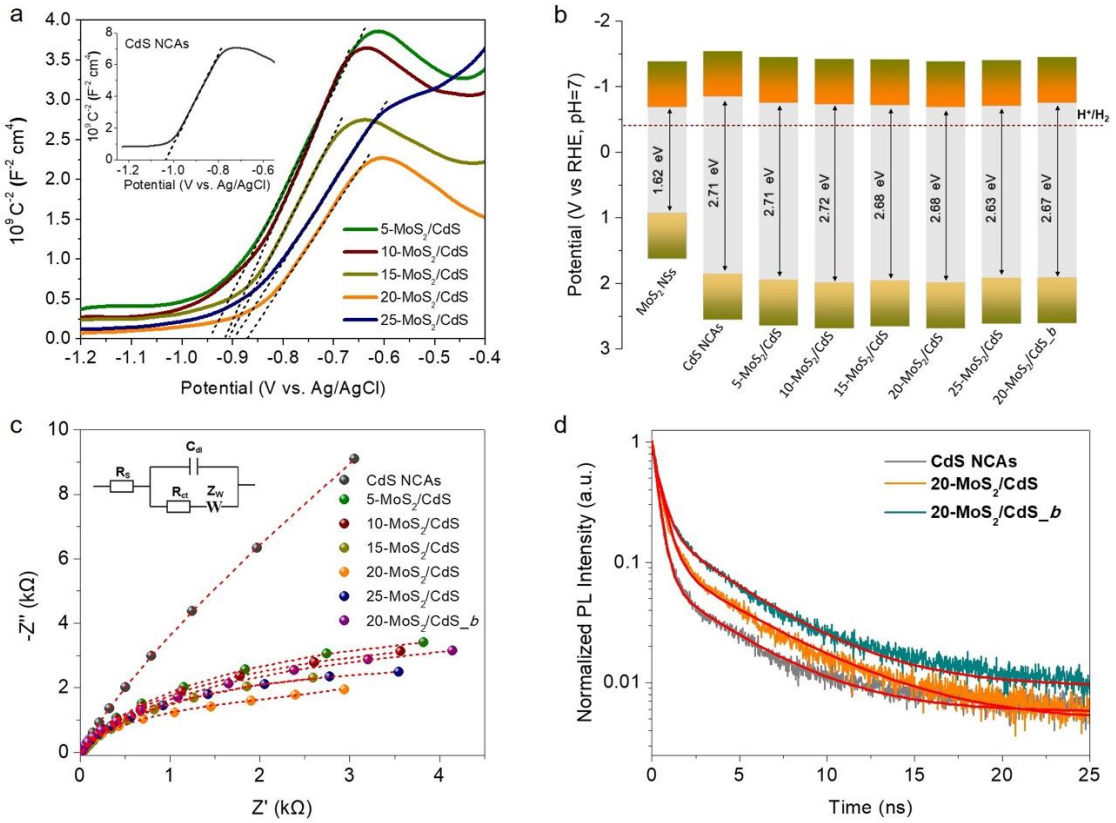

Figure 22. (a) Mott-Schottky plots of the MoS_2-modified CdS catalysts (inset: the Mott-Schottky plot of CdS NCAs). (b) Band-edge positions and (c) Nyquist plots for MoS_2 NSs, and CdS and MoS_2/CdS NCAs (Inset: equivalent circuit model $R_s[C_{dl}/(R_{ct} + Z_w])$. (d) Comparative time-resolved photoluminescence (TRPL) decay profiles of CdS NCAs and MoS_2-modified catalysts with 20 wt.% MoS_2 NSs (20-MoS_2/CdS) and MoS_2 bulk flakes (20-MoS_2/CdS_*b*).

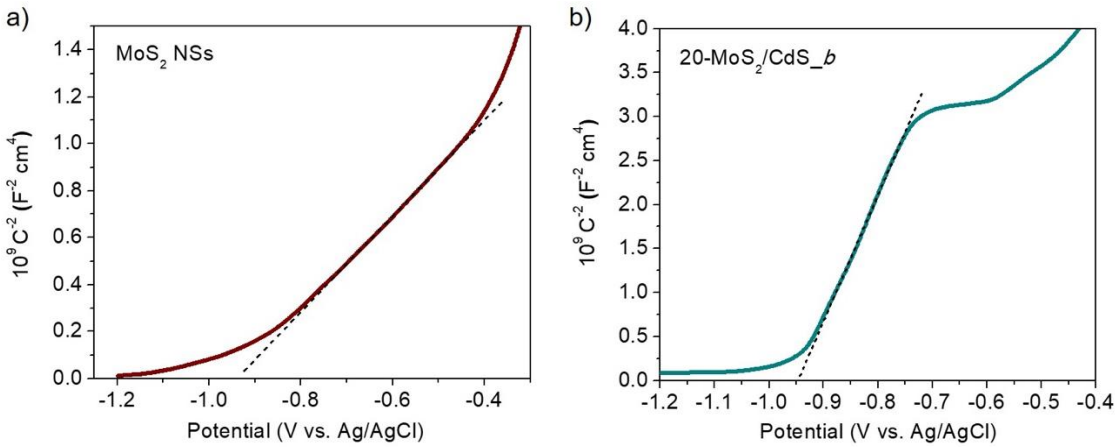

Figure 23. Mott-Schottky plots of (a) as-prepared MoS_2 NSs and (b) mesoporous 20-MoS_2/CdS_*b* catalyst.

Table 3. Electrochemical data obtained from EIS analysis for MoS_2 NSs and different mesoporous MoS_2-modified CdS catalysts.

Catalyst	E_{FB} (V vs. NHE, pH=7)	E_{VB} (V vs. NHE, pH=7)	Donor density (N_D, cm^{-3})	R_{ct} (kΩ)
MoS_2 NSs	–0.68	0.94	6.89×10^{17}	0.8
CdS NCAs	–0.84	1.87	5.87×10^{16}	13.5
5-MoS_2/CdS	–0.75	1.96	1.17×10^{17}	6.3
10-MoS_2/CdS	–0.72	2.00	1.22×10^{17}	5.6
15-MoS_2/CdS	–0.71	1.97	1.43×10^{17}	5.3
20-MoS_2/CdS	–0.68	2.00	1.70×10^{17}	2.7
25-MoS_2/CdS	–0.69	1.94	1.65×10^{17}	4.5
20-MoS_2/CdS_*b*	–0.75	1.92	1.13×10^{17}	5.2

Table 4. EIS equivalent circuit fitted parameters of pristine and MoS_2-modified CdS catalysts.

Sample	R_s (Ω)	C_{dl} (F)	R_{ct} (kΩ)	Zw ($k\Omega\bullet s^{-1/2}$)	x^2
MoS_2 NSs	9.33	43.65×10^{-6}	0.8	0.4	3.4×10^{-4}
CdS NCAs	21.90	16.99×10^{-6}	13.5	61.9	3.8×10^{-5}
5-MoS_2/CdS	17.23	21.84×10^{-6}	6.3	3.6	4.6×10^{-4}
10-MoS_2/CdS	18.38	23.05×10^{-6}	5.6	3.6	5.3×10^{-4}
15-MoS_2/CdS	26.52	40.36×10^{-6}	5.3	1.7	3.1×10^{-5}
20-MoS_2/CdS	14.03	17.72×10^{-6}	2.7	3.5	9.7×10^{-4}
25-MoS_2/CdS	11.64	20.91×10^{-6}	4.5	3.1	5.5×10^{-4}
20-MoS_2/CdS_*b*	9.79	17.70×10^{-6}	5.2	4.5	6.8×10^{-4}

It is worth mentioning that among all studied samples, 20-MoS_2/CdS NCAs catalyst exhibited the lowest charge-transfer resistance (~2.7 kΩ), which correlates well with its remarkable photocatalytic H_2 evolution performance. Also, the bulk reference catalyst (20-MoS_2/CdS_*b*) showed a relatively higher R_{ct} value (~5.2 kΩ), suggesting more sluggish charge transfer kinetics even though having similar MoS_2 content (20 wt.%) with its nanostructured analogue. These results explicitly indicate that the nanoscale size of MoS_2 layers has a prominent impact on the charge-transfer and separation dynamics at the MoS_2/CdS interface. This is also elaborated by photoluminescence (PL) study of catalysts under 375 nm excitation wavelength. As shown in Figure **24**, the 20-MoS_2/CdS catalyst has a lower PL intensity (at ~460 nm corresponding to the near band-edge excitonic emission) compared to the pristine CdS and bulk 20-MoS_2/CdS_*b* samples, indicating an improved electron-hole separation efficiency at the nanoscale MoS_2/CdS junctions. The carrier lifetime kinetics were also investigated using time-resolved photoluminescence (TRPL) spectroscopy and the obtained PL lifetime decay spectra are shown in Figure **22d**. To extract the PL lifetimes, we used a biexponential decay model [$F(t) = y_o + \sum_i \alpha_i e^{-t/\tau_i}$, i = 1, 2] to fit the PL decay curves, where α_i denote the amplitude fractions ($\sum_i \alpha_i = 1$) and τ_i is the carrier lifetime; the fitting parameters of this analysis are listed in Table **5**. This analysis yields an average lifetime (τ_{av}) of 3.12, 4.15 and 3.46 ns for mesoporous CdS, 20-MoS_2/CdS and 20-MoS_2/CdS_*b* NCAs catalysts, respectively. The TRPL results explicitly indicate that the nanoscale MoS_2/CdS junctions has a prominent impact on the charge-transfer kinetics at the catalyst interface, prolonging the electron lifetime and promoting a more efficient utilization of long-lived photoinduced electrons for H_2 evolution reaction, in line with the respective decrease of PL intensity in Figure **24**.

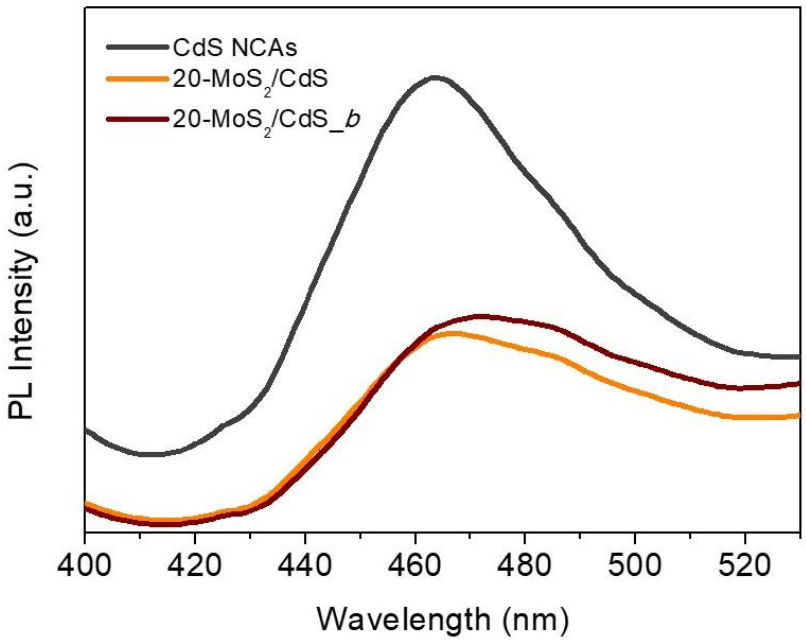

Figure 24. Room-temperature PL spectra of pristine and CdS NCAs modified with 20 wt.% of MoS_2 NSs (20-MoS_2/CdS) and MoS_2 microflakes (20-MoS_2/CdS_*b*). PL emission spectra were obtained at a concentration of 0.5 mg mL^{-1} in water with an excitation wavelength of 375 nm.

Table 5. PL lifetime biexponential decay model fitting parameters and calculated average lifetimes for the CdS, 20-MoS_2/CdS and 20-MoS_2/CdS_*b* NCAs.

Sample	**τ_1 (ns)**	**τ_2 (ns)**	**α_1 (%)**	**α_2 (%)**	**τ_{av}[a] (ns)**
CdS NCAs	0.35	3.97	77.6	22.4	3.12
20-MoS_2/CdS	0.51	4.85	64.8	35.2	4.15
20-MoS_2/CdS_*b*	0.49	4.09	63.8	36.2	3.46

[a]The average lifetime (τ_{av}) was calculated by the equation: $\tau_{av} = (\sum_i \alpha_i \tau_i^2)/(\sum_i \alpha_i \tau_i)$ (i = 1, 2).

This is also apparent in current density-voltage (J–V) data provided in Figure **25**, which indicate a substantially lower proton reduction potential (by 0.18 V) in MoS_2-modified catalysts compared to the pristine CdS. The observed positive shift in the

onset potential with MoS_2 deposition can be ascribed to the increased charge separation at the MoS_2/CdS interface and the lower energy barrier for H_2 evolution at the MoS_2 edge sites. Moreover, in comparison to the bulk reference catalyst (20-MoS_2/CdS_*b*), 20-MoS_2/CdS NCAs exhibited a quick current response, implying more rapid reaction kinetics caused by the low dimensionality of MoS_2 layers and increased amount of active MoS_2 edge-sites. For example, the current density at an applied voltage of –1.1 V versus Ag/AgCl is greatly enhanced from 0.65 mA cm^{-2} to 1.34 mA cm^{-2} with 20-MoS_2/CdS_*b* and 20-MoS_2/CdS catalyst, respectively.

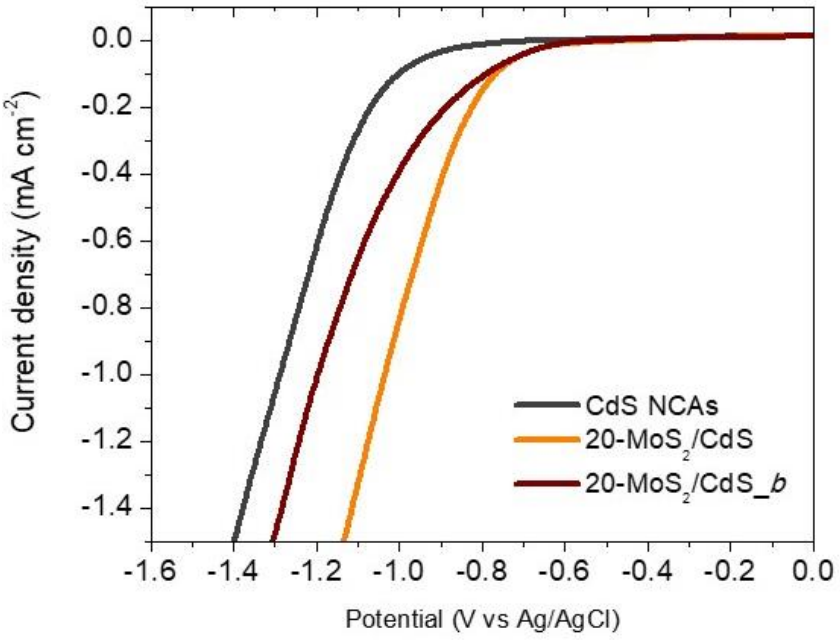

Figure 25. J–V plots of CdS, 20-MoS_2/CdS and 20-MoS_2/CdS_*b* NCAs.

Based on the above results, a possible reaction mechanism for the photocatalytic H_2 evolution reaction by MoS_2/CdS nanocatalysts was proposed, as shown in Scheme **1**. First, under light irradiation, both CdS and MoS_2 nanoparticles are excited and produce photogenerated carriers. Subsequently, because of the potential drop at the MoS_2/CdS interface, electrons are transferred from CdS into the CB of MoS_2, where they reduce protons to H_2. The smooth charge transfer and abated electron-hole recombination, which are effectively induced by the nanoscale MoS_2/CdS junctions, would provide

prolonged lifetime and thus more possibilities for electrons to engage in catalytic H_2 evolution. On the other, the photogenerated holes on the surface of CdS and/or MoS_2 oxidize the sacrificial reagents (such as S^{2-} and SO_3^{2-}). Such charge transfer pathways within the MoS_2/CdS nanojunction network are evidenced from EIS and TRPL studies.

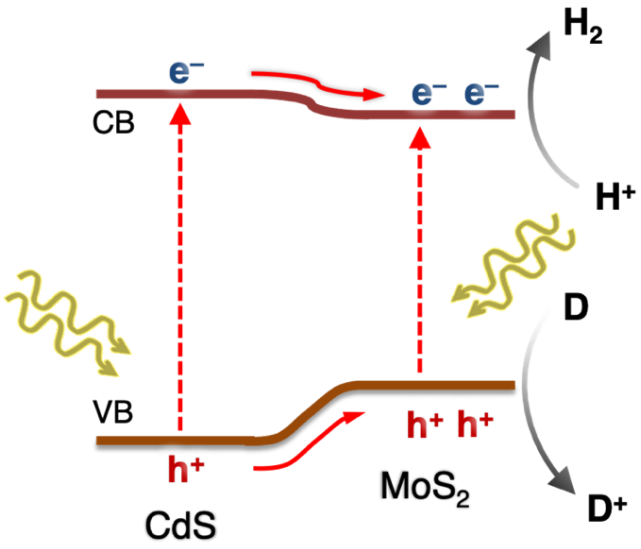

Scheme 1. Expected reaction mechanism for the photocatalytic H_2 evolution over mesoporous MoS_2/CdS NCAs under visible light irradiation.

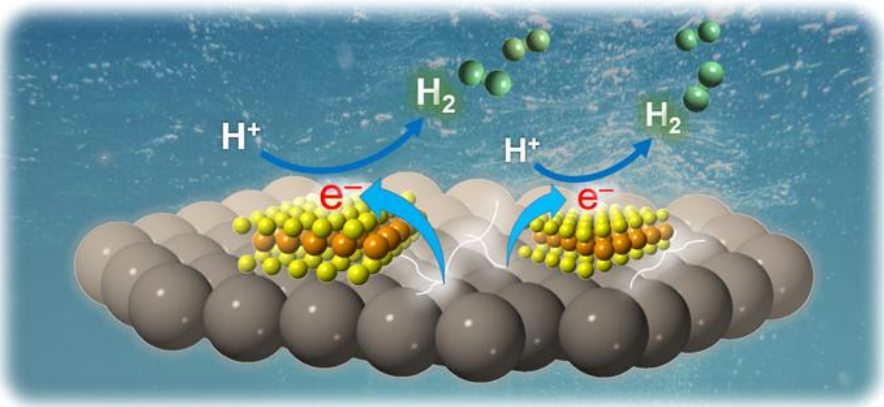

Scheme 2. Illustration of the photocatalytic H_2 evolution mechanism of mesoporous MoS_2/CdS NCAs (CdS in grey cycles and MoS_2 in yellow cycles).

5. Conclusion

In summary, nanojunction networks of CdS NCs and MoS_2 NSs with different composition have been successfully prepared by depositing MoS_2 NSs on the surface of mesoporous CdS NC assemblies. Thorough X-ray diffraction, electron microscopy and X-ray photoelectron spectroscopy measurements, the crystallinity and morphology of the prepared catalysts were confirmed. These heterostuctures exhibit high H_2 production efficiency which is promoted by their electronic band structure that allows a spatial dissociation of charge carriers across the MoS_2/CdS interface. Evidence for this was provided by electrochemical and photoluminescence studies. Owing to these characteristics, MoS_2/CdS catalyst with 20 wt.% MoS_2 content attains a 6.3× and 1.4× increase in H_2 production rate than bare mesoporous CdS and bulk MoS_2/CdS analogues, respectively. It also presents an energy conversion efficiency of 51.2% at 420 ± 10 nm, which is one of the highest reported for MoS_2-modified CdS catalysts. Moreover, MoS_2/CdS nanojunction networks exhibit persistent H_2 evolution activity after three 5-h recycling tests. The results of this study present an understanding of the charge transfer dynamics at the MoS_2/CdS nanoscale junctions and support the potential viability of the MoS_2-modified CdS nano-heterostructures as photocatalysts for clean energy conversion.

References

[1] Y. Cui, Z. Zhou, T. Li, K. Wang, J. Li, Z. Wei, *Adv. Funct. Mater.*, **2019**, 29.

[2] H. T. Tan, Y. Z. Feng, X. H. Rui, Y. Yu, S. M. Huang, *Small Methods*, **2020**, 4

[3] S. Manzeli, D. Ovchinnikov, D. Pasquier, O. V. Yazyev, A. Kis, *Nat Rev Mater*, **2017**,2

[4] C. Zhu, D. Gao, J. Ding, D. Chao, J. Wang, *Chem. Soc. Rev.*, **2018**, 47, 4332-4356.

[5] M. Chhowalla, H. S. Shin, G. Eda, L.-J. Li, K. P. Loh, H. Zhang, *Nature Chemistry*, **2013**, 5, 263-275.

[6] Y.-J. Yuan, D. Chen, Z.-T. Yu, Z.-G. Zou, *Journal of Materials Chemistry A*, **2018**, 6, 11606- 11630.

[7] S. Mukherjee, Z. Ren, G. Singh, *Nano-Micro Letters*, **2018**, 10.

[8] J. Yin, J. Jin, H. Lin, Z. Yin, J. Li, M. Lu, L. Guo, P. Xi, Y. Tang, C.-H. Yan, *Advanced Science*, **2020**,7.

[9] Y. Tachibana, L. Vayssieres, J. R. Durrant, *Nature Photon*, **2012**, 6, 511–518.

[10] A. Fujishima, K. Honda, *Nature*, **1972**, 238, 37-38.

[11] X. Lin, J. Yu, J. Low, Y. Fang, J. Xiao, X. Chen, *Journal of Materials Chemistry A*, **2015**, 3, 2485-2534.

[12] A. Kudo and Y. Miseki, *Chem. Soc. Rev.*, 2009, **38**, 253–278.

[13] I. Vamvasakis, K. S. Subrahmanyam, M. G. Kanatzidis, G. S. Armatas, *ACS Nano*, **2015**, 9, 4419-4426.

[14] I. Vamvasakis, A. Trapali, J. Miao, B. Liu, G. S. Armatas, *Inorg. Chem. Front.*, **2017**, 4, 433-441.

[15] I. Vamvasakis, B. Lui, G. S. Armatas, *Adv. Funct. Mater.*, **2016**, 26, 8062-8071.

[16] I. Vamvasakis, I. Papadas, T. Tzanoudakis, C. Drivas, S. A. Choulis, S. Kennou, G. S. Armatas, *ACS Catalysis.*, **2018**, 8, 8726-8738.

[17] S. Pathan, A. Patel, *Dalton Trans.*, **2011**, 40, 348-355.

[18] E. D. Koutsouroubi I. Vamvasakis, I. Papadas, C. Drivas, S. S. Choulis, S. Kennou, G. S. Armatas, *ChemPlusChem*, **2020**,85 1379-1388.

[19] J. Yuan, J. Wen, Q. Gao, S. Chen, J. Li, X. Li, Y. Fang, *Dalton Trans.*, **2015**, 44, 1680–1689.

[20] N. Y. Cui, N. M. D. Brown, A. McKinley, *Appl. Surf. Sci.*, **1999**, 151, 17-28.

[21] P. A. Spevack, N. S. McIntyre, *J. Phys. Chem*., **1993**, 97, 11031-11036.

[22] A. Syariati, S. Kumar, A. Zahid, A. Ali El Yumin, J. Ye and P. Rudolf, *Chem. Commun.*, **2019**, 55, 10384-10387.

[23] Barreca, D.; Gasparotto, A.; Maragno, C.; Tondello, *Surf. Sci. Spectra*, **2002**, 9, 46–53.

[24] M. Thommes, *Chemie Ingenieur Technik*, **2010**, 82, 1059–1073.

[25] P.L. Ravikovitch, D. Wei, W. T. Chueh, G. L. Haller, *J. Phys. Chem. B*, **1997**, 101, 3671−3679.

[26] N. Buehler, K. Meier, and J. F. Reber, *J. Phys. Chem.*, **1984**, 88, 3261–3268.

[27] X. Zong, H. Yan, G. Wu, G. Ma, F. Wen, L. Wang, C. Li, *J. Am. Chem. Soc.*, **2008**, 130, 7176-7177.

[28] X. Zong, H. Yan, G. Wu, G. Ma, F. Wen, L. Wang, C. Li, *J. Phys. Chem. C*, **2010**, 114, 1963–1968.

[29] G. Chen, D. Li, F. Li, Y. Fan, H. Zhao, Y. Luo, R. Yu, Q. Meng, *Applied Catalysis A: General*, **2012**, 443-444, 138-144.

[30] X. Y. Liu, H. Yu, X. Quan, S. Chen, *International Journal of Photoenergy*, **2013**, 2013, 1-5.

[31] J. Zhang, Z. Zhu, X. Feng, *Chem. Eur. J*., **2014**, 20, 10632–10635.

[32] J. Xiong, Y. Liu, D. Wang, S. Liang, W. Wu, L. Wu, *J. Mater. Chem. A*, **2015**, 3, 12631–12635.

[33] K. Chang., M. Li, T. Wang, S. Ouyang, P. Li, L. Liu, J. Ye, *Adv. Energy Mater*, **2015**, 5.

[34] J. Xu, X. Cao, *Chemical Engineering Journal*, **2015**, 260, 642-648.

[35] D. Lang, T. Shen, Q. Xiang, *ChemCatChem*, **2015**, 7, 943-951.

[36] F. Ma, Y. Wu, Y. Shao, Y. Zhong, J. Lv, X. Hao, *Nano Energy*, **2016**, 27, 466-474.

[37] J. He, L. Chen, F. Wang, Y. Liu, P. Chen, C.-T. Au, S.-F. Yin, *ChemSusChem*, **2016**, 9, 624-630.

[38] X. Zhou, J. Huang, H. Zhang, H. Sun, W. Tu, *International Journal of Hydrogen Energy*, **2016**, 41, 14758-14767.

[39] X. Yin, L. Leilei, W.-J. Jiang, Y. Zhang, X. Zhang, L.-J. Wan, J.-S. Hu, *ACS Appl. Mater. Interfaces*, **2016**, 8, 15258-15266.

[40] D. P. Kumar, S. Hong, D. A. Reddy, T. K. Kim, *J. Mater. Chem. A*, **2016**, 4, 18551–18558.

[41] S. Ma, J. Xie, J. Wen, K. He, X. Li, W. Liu, X. Zhang, *Applied Surface Science*, **2017**, 391, 580-591.

[42] A. Wu, C. Tian, Y. Jiao, Q. Yan, G. Yang, H. Fu, *Applied Catalysis B: Environmental*, **2017**, 203, 955-963.

[43] X. Hai, W. Zhou, S. Wang, H. Pang, K. Chang, F. Ichihara, J. Ye, *Nano Energy*, **2017**, 39, 409-417.

[44] S. Zhang, H. Yang, H. Gao, R. Cao, J. Huang, X. Xu, *ACS Appl Mater Interfaces*, **2017**, 9, 23635–23646.

[45] L. Zhao, J. Jia, Z. Yang, J. Yu, A. Wang, Y. Sang, W. Zhou, H. Liu, *Applied Catalysis B: Environmental*, **2017**, 210, 290-296.

[46] B. Chai, M. Xu, J. Yan, Z. Ren, *Applied Surface Science*, **2018**, 430, 523-530

[47] L. Jiang, L. Wang, G. Xu, L. Gu, Y. Yuan, *Sustainable Energy Fuels*, **2018**, 2, 430-435.

[48] J. Sun, L. Duan, Q. Wu, W. Yao, *Chemical Engineering Journal*, **2018**, 332, 449-455.

[49] X.-H. Zhang, N. Li, J. Wu, Y.-Z. Zheng, X. Tao, *Applied Catalysis B: Environmental*, **2018**, 229, 227-236.

[50] Z.-W. Zhang, Q.-H. Li, X.-Q. Qiao, D. Hou, D.-S. Li, *Chinese Journal of Catalysis*, **2019**, 40, 371-379.

[51] X. Li, X. Lv, N. Li, J. Wu, Y.-Z. Zheng, X. Tao, *Applied Catalysis B: Environmental*, **2019**, 243, 76-85.

[52] W. Zhao, J. Liu, Z. Ding, J. Zhang, X. Wang, *Journal of Alloys and Compounds*, **2020**, 813.

[53] M. Xiong, J. Yan, B. Chai, G. Fan, G. Song, *Journal of Materials Science & Technology*, **2020**, 56, 179-188.